

**Key Points:**

- Highest age-elevation thermochronology profile from the Andes at Cerro Mercedario
- Apatite and zircon (U-Th-Sm)/He dates and inverse thermal history modeling show 22–10 Ma thrust driven exhumation of the La Ramada massif
- Growth of Frontal Cordillera basement culmination feeds slip into eastward adjacent Precordillera during propagation of an east-vergent orogenic wedge

**Supporting Information:**

Supporting Information may be found in the online version of this article.

**Correspondence to:**

C. J. Howlett,  
[cadenhowlett@arizona.edu](mailto:cadenhowlett@arizona.edu)

**Citation:**

Howlett, C. J., Ronemus, C. B., Carrapa, B., & DeCelles, P. G. (2025). Miocene construction of the High Andes recorded by exhumation of the Frontal Cordillera, La Ramada massif of western Argentina (32°S). *Tectonics*, *44*, e2024TC008433. <https://doi.org/10.1029/2024TC008433>

Received 28 MAY 2024

Accepted 8 JAN 2025

**Author Contributions:**

**Conceptualization:** C. J. Howlett, C. B. Ronemus, B. Carrapa, P. G. DeCelles  
**Data curation:** C. J. Howlett  
**Formal analysis:** C. J. Howlett  
**Funding acquisition:** B. Carrapa, P. G. DeCelles  
**Investigation:** C. J. Howlett, C. B. Ronemus, B. Carrapa, P. G. DeCelles  
**Methodology:** C. J. Howlett  
**Resources:** B. Carrapa, P. G. DeCelles  
**Software:** C. J. Howlett  
**Supervision:** B. Carrapa, P. G. DeCelles  
**Writing – original draft:** C. J. Howlett  
**Writing – review & editing:** C. J. Howlett, C. B. Ronemus, B. Carrapa, P. G. DeCelles

## Miocene Construction of the High Andes Recorded by Exhumation of the Frontal Cordillera, La Ramada Massif of Western Argentina (32°S)

C. J. Howlett<sup>1</sup> , C. B. Ronemus<sup>1</sup> , B. Carrapa<sup>1</sup>, and P. G. DeCelles<sup>1</sup> 

<sup>1</sup>Department of Geosciences, University of Arizona, Tucson, AZ, USA

**Abstract** The Frontal Cordillera is a first-order geologic feature of the southern central Andes, hosting the highest hinterland topography above the modern Pampean flat-slab segment. The timing of Frontal Cordillera exhumation is important for testing models of Andean tectonics, yet large latitudinal gaps exist between structural and thermochronological constraints for the region. We conducted a thermochronometric study using a 4.4 km age-elevation transect along the northeast ridge of Cerro Mercedario, the highest peak in the La Ramada massif at ~32°S. Zircon (U-Th)/He dates indicate partial resetting, supporting a limited magnitude of exhumation in even the most extreme Andean topography. Single grain apatite (U-Th-Sm)/He dates range from  $8.5 \pm 0.9$  to  $35.8 \pm 3.6$  Ma, with median dates of ~10.5 to ~15.7 Ma with increasing elevation. Integrated with geologic mapping and thermal history modeling, these data suggest Early to Middle Miocene exhumation along the Santa Cruz and Espinacito faults concomitant with uplift of the La Ramada massif. New apatite helium data from the Cordillera del Tigre segment of the Frontal Cordillera are partially reset and preferred modeling interpretations suggest exhumation ca. 11–9 Ma, coeval with shortening in the eastward adjacent Precordillera. These data add to accumulating regional evidence for out-of-sequence deformation during the Miocene, consistent with internal (hinterland) growth of a subcritical orogenic wedge contemporaneous with surface uplift and crustal thickening in the south-central Andes.

**Plain Language Summary** The convergence of tectonic plates causes rocks to bend, break, pile up, and rise to high elevations. As mountains like the Andes of South America rise, they get worn down by rain, wind, ice, and gravity. Geologists can analyze elements in rocks to determine when erosion happened, which tells us when mountains were growing. This is important because the timing of topographic growth is critical to understanding things like the evolution of life and the long-term behavior of Earth's climate. For this study, we collected rock samples from one of the highest mountains in the Andes (Argentina's Cerro Mercedario) to figure out when uplift and erosion were happening. Sampling at high elevation is a powerful approach because the highest rocks usually reach Earth's surface first, recording the earliest phases of mountain building. We found that the high peaks started rising around 20 million years ago, coeval with regional thickening and uplift of South American crust. In addition, our data show that Cerro Mercedario was still being uplifted after contractional deformation had moved east to near the city of San Juan, adding evidence that the Earth's crust doesn't always break in a sequential, migrating fashion as predicted by idealized models of mountain belts.

### 1. Introduction

The highest Andes are located along the Argentina-Chile border between 31.5° and 32.5°S, above a shallowly subducting segment of Nazca oceanic lithosphere (Figure 1). Extreme elevation in this region is accompanied by a modern crustal thickness exceeding 65 km (e.g., Cristallini & Ramos, 2000; Gans et al., 2011; Tassara & Echaurren, 2012). Crustal thickness values are comparable to those in the Altiplano orogenic plateau to the north despite a two-fold decrease in upper crustal shortening from north to south (e.g., Allmendinger et al., 1990; Anderson et al., 2018; Giambiagi et al., 2012, 2022; McQuarrie, 2002). The timing and mechanism(s) of crustal thickening and surface uplift in Cordilleran orogenic systems remain first-order questions that are particularly relevant in this transitional segment of the south-central Andes (Carrapa et al., 2022; Hoke et al., 2014; Horton, 2018; Introcaso et al., 1992). Investigating these relationships require constraints on the timing, rates, and patterns of rock uplift and exhumation in the upper plate (e.g., Anderson et al., 2018; Hoke et al., 2015). To this end, numerous studies have used the synorogenic basin record and bedrock geo- and thermochronology to gain insight into the deformation chronology at the latitude of interest (Alarcón & Pinto, 2015; Buelow et al., 2018;

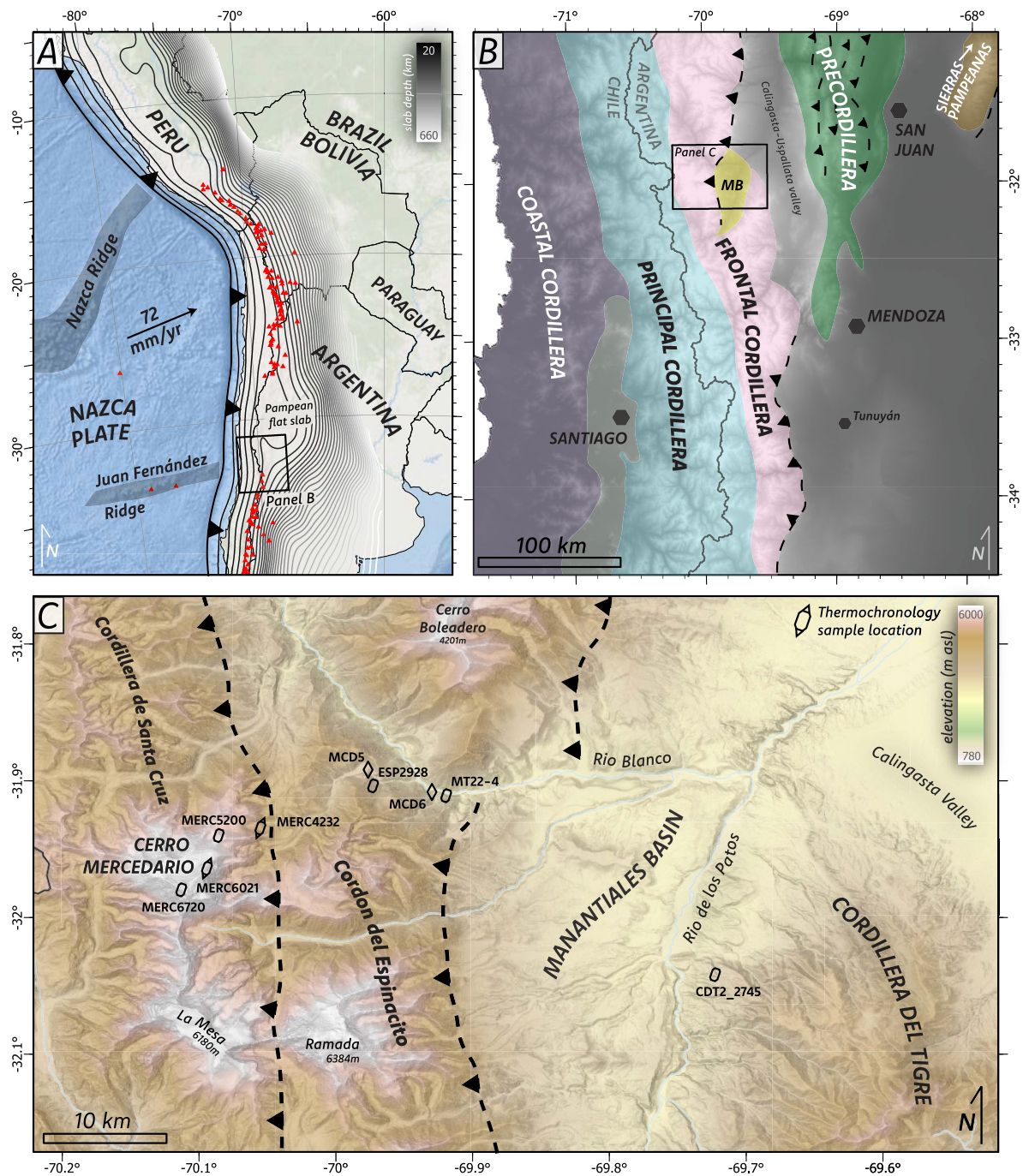


**Figure 1.** (a) Plate tectonic context of central and south-central Andes, with subducted slab depth contours in black and active volcanoes related to the magmatic arc as red triangles. Slab contours—ranging from 20 to 660 km with an interval of 20 km—are from Hayes et al. (2018). (b) Generalized tectonomorphic/structural provinces of the south-central Andes. MB—Manantiales Basin (c) Topography and major structures of the Frontal Cordillera at ~32°S, with thermochronology sample locations from this study shown as black symbols (rectangles—apatite (U-Th-Sm)/He; diamonds—zircon (U-Th)/He; combined—double dated). Western (Espinacito and Santa Cruz) and eastern (Cordillera del Tigre) segments of the Frontal Cordillera separated by the Eocene-Miocene Manantiales wedge-top basin.

Cristallini & Ramos, 2000; Dávila et al., 2007, 2010; Fosdick et al., 2024; Jordan et al., 1996; Mackaman-Lofland et al., 2020, 2024; Maydagán et al., 2020; Suriano et al., 2017, 2023). Despite these efforts, uncertainty surrounds the tectono-thermal evolution of the Frontal Cordillera, a dominant structural and topographic component of the orogenic system at this latitude (e.g., Lossada et al., 2018; Mazzitelli, 2020) (Figure 1).

The timing of Frontal Cordillera exhumation is the focus of studies that make dramatically different interpretations about the overall tectonic architecture of the south-central Andes (e.g., Hoke et al., 2014; Lossada et al., 2023; Riesner et al., 2019). For example, “early” uplift of the Frontal Cordillera (ca. 20 Ma) prior to deformation in the westward adjacent Principal Cordillera (Figure 1a) has been used as evidence for an overall west-vergent Andean system (Riesner et al., 2019). Other constraints—although suggesting similar timing—are interpreted to be consistent with the “paradigm” of an eastward propagating orogenic wedge (Hoke et al., 2014). Therefore, determining the thermal history and, in particular, the regional patterns of Frontal Cordillera uplift and exhumation is crucial for refining models of mountain building in the south-central Andes.

Extreme topography and its location relative to existing data sets make the La Ramada massif of western Argentina an ideal locality for a thermochronological study (Figure 1b). Here, we integrate new field observations with the highest systematic thermochronology date-elevation transect from the Andes to address exhumation timing and magnitude at Cerro Mercedario (6,720 m asl). Our results indicate limited Cenozoic erosion that, combined with active shortening, supports significant uplift and crustal thickening during the Miocene. We consider our results alongside thermal history inversions of existing thermochronology transects from the Frontal Cordillera with variable cooling histories. The along-strike discrepancy in the timing of Frontal Cordillera exhumation and regional east-west patterns in the timing of deformation have implications in the context of Andean orogenic wedge behavior, providing insights into the processes and mechanisms that form some of the highest topography in the Andes and other cordilleran-type orogenic systems.

## 2. Tectonic Setting and Geologic Background

In strongly convergent plate tectonic settings, the subduction of oceanic lithosphere beneath a continent creates a predictable arrangement of geologic features at the surface, collectively referred to as a cordilleran orogenic system. The south-central Andes (Figure 1a) are the archetypical example of this, hosting (from west to east) a subduction trench, forearc basin, a magmatic arc, retroarc fold-thrust belt, and a regional foreland basin system. Between 28° and 33°S, the Pampean flat-slab segment of the Nazca Plate has ruptured the foreland region and extinguished the modern magmatic arc (Figure 1a; Cahill & Isacks, 1992; Ramos et al., 2002). Above the flat-slab zone at ~32°S, the orogen is subdivided into five tectonomorphic provinces on the basis of lithology and structural style: the Coastal Cordillera in Chile, the Principal and Frontal Cordilleras along the Argentina/Chile border, the Argentine Precordillera, and the Sierras Pampeanas (Figure 1b; Ramos et al., 1996).

At the study latitude, the Principal and Frontal Cordilleras together host the most extreme relief and highest topography in the Andes (referred to here as the High Andes), with average elevations exceeding 4 km and numerous peaks rising >6,000 m asl (Figure 1c). The Principal Cordillera consists primarily of Mesozoic-Cenozoic sedimentary and volcanic deposits deformed in a thin-skinned style above a detachment in Jurassic gypsum, while the Frontal Cordillera is characterized by basement blocks of Permo-Triassic plutonic and volcanic rock exhumed along west-dipping high-angle reverse faults that likely root into the mid- to lower crust (Cristallini & Ramos, 2000). Collectively, these two zones comprise the hybrid thin- and thick-skinned portion of the orogenic wedge known as the La Ramada fold-thrust belt (e.g., Cristallini & Ramos, 2000; Mackaman-Lofland et al., 2020). The hybrid character and exhumed basement blocks that comprise the highest peaks of the Frontal Cordillera are likely the result of reactivation and tectonic inversion of a Late Triassic rift system (Alvarez & Ramos, 1999; Cristallini & Ramos, 2000). A major jog in the location of the Frontal Cordillera occurs at the latitude of the study area, centered around the Eocene-Middle Miocene Manantiales basin (Figures 1b and 1c). The Manantiales basin contains a >4 km thick succession of mainly Early-Middle Miocene nonmarine sedimentary rocks (e.g., Pinto et al., 2018; Ronemus et al., 2024), with its western margin overthrust by the Santa Cruz and Espinacito fault system and eastern margin bound by the Cordillera del Tigre segment of the Frontal Cordillera (Figures 1c and 2a; Pérez, 1995; Jordan et al., 1996). Uplift timing of each bounding segment has implications for the interpreted deposition “zone” within the Andean foreland basin system (i.e., foredeep vs. wedgetop *sensu* DeCelles & Giles, 1996). Jordan et al. (1996) suggested the Manantiales basin may have accumulated in a wedgetop position; although this wasn't their preferred interpretation, new sedimentology from Ronemus et al. (2024) supports this scenario, which we expand on in this work.

Several studies have improved our understanding of the timing of uplift and exhumation of the Frontal Cordillera and the broader deformation chronology at this latitude. Previous studies determined a generally eastward migration of deformation, beginning as early as ca. 100 Ma in the western regions and propagating into the

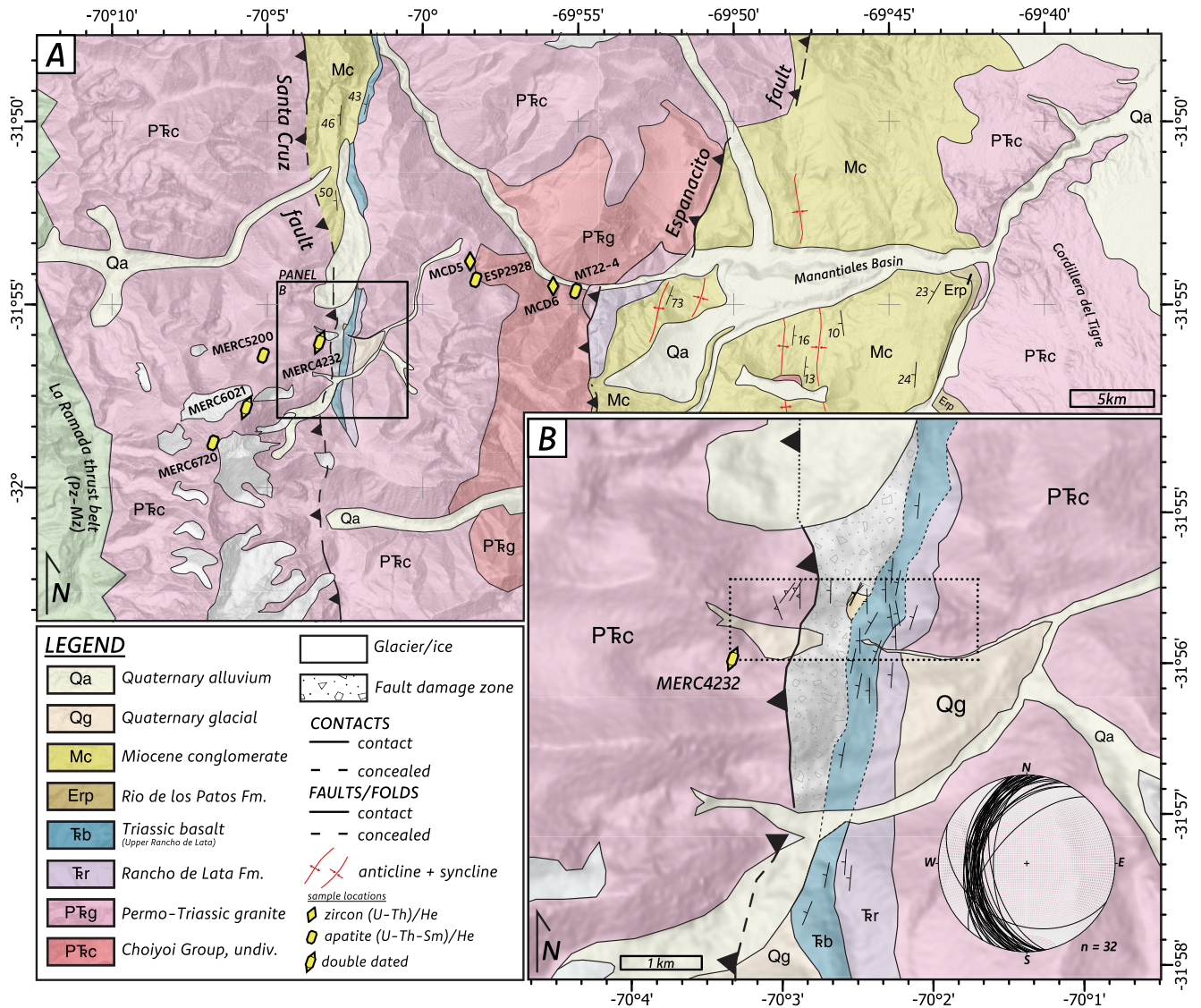


**Figure 2.** (a) Geologic mapping results from this study and Ronemus et al. (2024). (b) Map of Santa Cruz fault zone, with Lambert equal area stereonet showing consistent westward bed dip of Triassic sandstone and basalt units. Overlapping structural measurements of similar orientation were averaged for clarity. Dotted black rectangle denotes location of panorama in Figure 3a.

Principal and Frontal Cordilleras by 21–18 Ma (Giambiagi et al., 2022). The timing of deformation in the Principal and Frontal Cordilleras has been constrained primarily by the Cenozoic sedimentary basin record (Levina et al., 2014; Pérez, 1995; Ronemus et al., 2024; Suriano et al., 2023) and there were no thermochronology constraints on the westward adjacent basement block uplifts prior to this study. Existing thermochronology data from Frontal Cordillera basement to the northwest of our study area have been interpreted to record rapid cooling pulses in the early Cenozoic (ca. 60–30 Ma) and from 15 to 10 Ma (Lossada et al., 2017, 2020a, 2020b; Mackaman-Lofland et al., 2024; Maydagán et al., 2020). Approximately 100 km south of the La Ramada massif, low-temperature thermochronology and basin analysis has constrained the main-phase of Frontal Cordillera exhumation to the mid-Miocene (Buelow et al., 2018; Hoke et al., 2014; Lossada et al., 2020a, 2020b, 2023; Riesner et al., 2019). Near Cerro Aconcagua at 32.5°S, shortening, exhumation and crustal thickening in the Principal Cordillera and Aconcagua fold and thrust belt occurred primarily at ~15–12 Ma (e.g., Carrapa et al., 2022; Giambiagi et al., 2012), with possible deformation pulses as early as the Late Cretaceous (Fennell et al., 2023).

East of our study area, deformation in the Precordillera began ca. 18 Ma and continued until ca. 2 Ma (e.g., Fosdick et al., 2015; Levina et al., 2014), contemporaneous with out-of-sequence thrusting in the La Ramada massif (e.g., Ronemus et al., 2024; this study). Orthogonal subduction of the Juan Fernandez ridge and shallowing of the subducted slab began by ca. 11 Ma, eventually extinguishing the magmatic arc and uplifting the Sierras Pampeanas mostly during the Late Miocene (Ramos et al., 2002; Stevens Goddard et al., 2018).

### 3. Methods and Results

#### 3.1. Geologic Mapping and Field Observations

Geologic mapping (Figure 2) was conducted at 1:50,000 scale atop 100-m contours and MapBox satellite imagery using the FieldMove iPad application. Mapping focused on the Santa Cruz fault zone, a west-dipping basement-involved reverse fault that is hypothesized to have uplifted the highest peaks of the La Ramada massif (e.g., Lencinas, 1982). The fault zone is well exposed near the northeast ridge of Cerro Mercedario and is characterized by a hanging wall of Choiyoi Group granite and rhyolite in thrust contact with an ~350 m thick panel of west-dipping (~35°) sedimentary and volcanic strata (Figures 2b and 3a).

The lowermost sedimentary unit is composed of interbedded red siltstone and medium to coarse-grained sandstone beds, which have been previously mapped as the Triassic Rancho de Lata Formation (Alvarez et al., 1995; Cristallini & Ramos, 2000). These beds are capped by a highly altered black basalt with abundant zeolite and quartz-filled vesicles (Figure 3d), previously mapped as Jurassic sandstones or limestones (Cristallini & Ramos, 2000; Mazzitelli, 2020) but herein assigned to the Rancho de Lata Formation based on similarity to previous lithologic descriptions (Alvarez & Ramos, 1999). The Santa Cruz fault is characterized by a 300 m thick damage zone with indications of extensive hydrothermal alteration, including the alteration of olivine to iddingsite in the upper Rancho de Lata basalt flows (Figure 3e). In the westernmost portion of the fault zone, we document a folded pebble-cobble clast-supported conglomerate (Figure 3b). Previous regional-scale maps portray this outcrop as Miocene in age (e.g., Tedesco et al., 2024), equivalent to the eastward adjacent Chinchas Formation that comprises most of the Manantiales basin fill. If this interpretation is correct, the folding of this unit provides evidence of Cenozoic (perhaps Middle Miocene) uplift along the Santa Cruz fault.

#### 3.2. (U-Th-Sm)/He Thermochronology

##### 3.2.1. Thermochronology Methods

Low-temperature thermochronology is a useful tool for determining the time at which a mineral cools through a given temperature window in the upper crust and can be used as a proxy for timing/depth of erosion or to date tectonic exhumation (in extensional settings) (e.g., Braun et al., 2006). The (U-Th-Sm)/He thermochronometer relies on thermally activated diffusion of radiogenic  $^4\text{He}$  produced during the decay of radioactive  $^{238}\text{U}$ ,  $^{235}\text{U}$ ,  $^{232}\text{Th}$ , and  $^{147}\text{Sm}$  in apatite and zircon (Farley & Stockli, 2002). The nominal range of temperatures over which  $^4\text{He}$  diffusion occurs (known as the partial retention zone, or PRZ) is ~200–160°C and ~80–55°C for zircon and apatite, respectively (Reiners & Brandon, 2006). Detailed analytical methods for zircon and apatite helium thermochronometry (ZHe and AHe) are reported in Supporting Information S1 (Text S1).

The relationship between thermochronometric date and elevation for samples collected over significant relief is a powerful strategy for constraining the timing and rates of rock exhumation (e.g., Fitzgerald et al., 1995; Huntington et al., 2007; Reiners et al., 2004). Specifically, the slope of an age-elevation trend provides information about the rate of exhumation, defined as the displacement of rocks with respect to Earth's surface which is equivalent to the amount of material removed from the surface (e.g., England & Molnar, 1990). Furthermore, vertical profiles can be jointly modeled using inverse thermal history modeling techniques to obtain statistically more robust thermal histories (e.g., Gallagher, 2012; Ketcham, 2024).

We measured (U-Th-Sm)/He dates on six apatite samples (5 single grains per sample for a total of 30 single grain dates) and four zircon samples (20 single grain dates) collected along an ~4.4 km vertical transect up the northeast ridge of Cerro Mercedario (Figures 1c and 4; Tables 1 and 2). This age-elevation profile represents the highest relief profile available from the Andes. Two AHe samples and two ZHe samples were collected in the hanging wall of the Espinacito fault (below the Santa Cruz fault) and four samples were collected from the hanging wall of the Santa Cruz fault (Figure 2). Two of the samples from the hanging wall of the Santa Cruz fault were double-dated using both AHe and ZHe. An additional sample collected from the Cordillera del Tigre portion of the

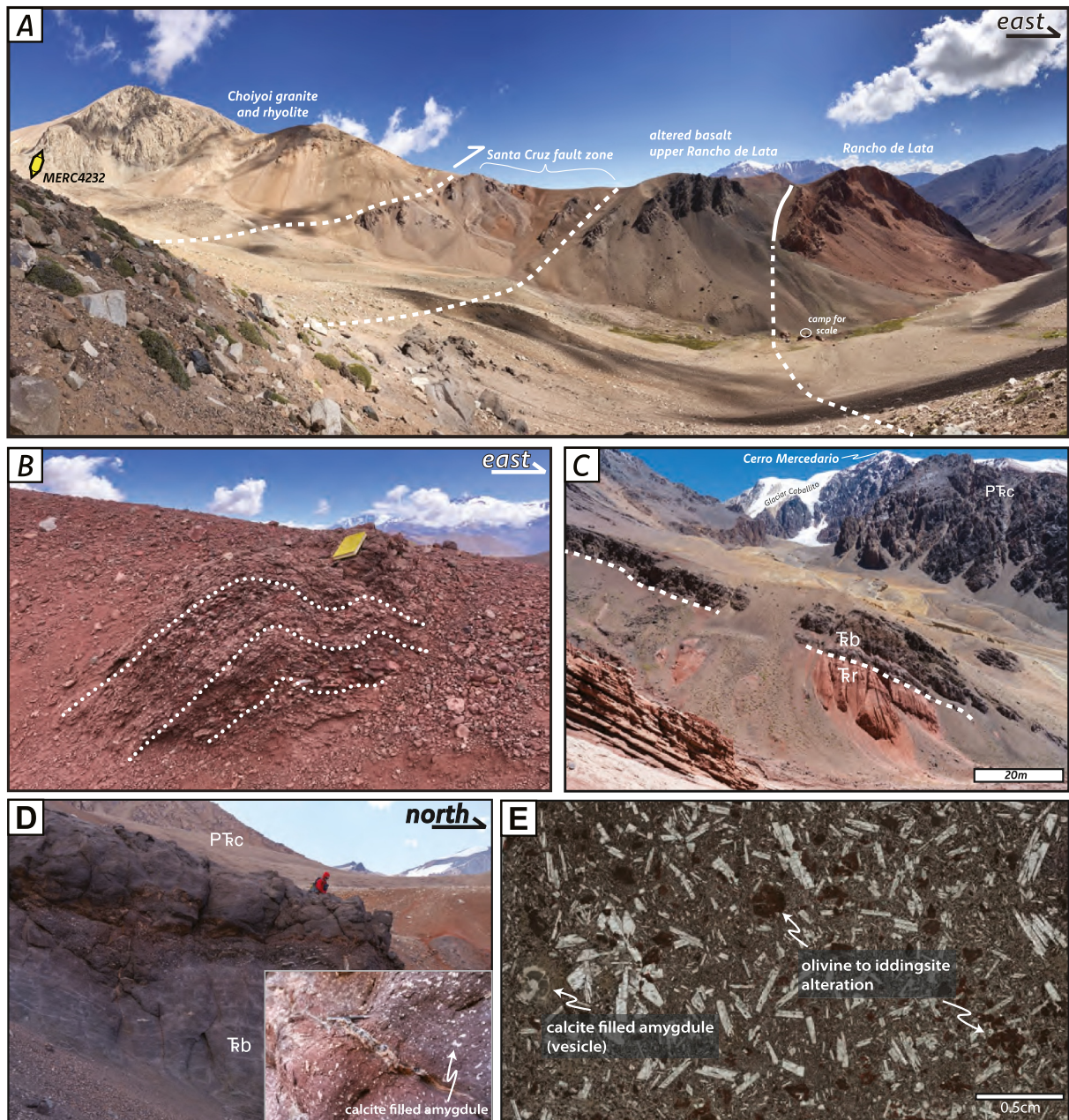


**Figure 3.** Field observations from the Santa Cruz fault zone along the eastern face of Cerro Mercedario. (a) Primary structural relationship along Santa Cruz fault, with Choyoi Group in thrust contact with (b) folded Miocene (?) pebble-cobble conglomerate within the Santa Cruz fault zone. Notebook for scale. (c) Eastern face of Cerro Mercedario, displaying the planar contact between red sandstone and overlying altered basalt. (d) Altered basalt showing extensive evidence of alteration related to the Santa Cruz fault, with inset showing a close up of zeolite and quartz-filled vesicles. (e) Thin section photomicrograph representative of black basalt with filled vesicles and evidence of hydrothermal alteration of olivine.

Frontal Cordillera on the eastern side of the Manantiales Basin was analyzed for AHe (Figure 1c). Samples were collected from Permo-Triassic (ca. 290–225 Ma) biotite granites and porphyritic rhyolites of the Choyoi Group, the dominant lithologies of the Frontal Cordillera structural province (e.g., Dahlquist et al., 2024; Mackaman-Lofland et al., 2019; Mpodozis & Kay, 1992). All samples were hand-picked and irradiated for apatite fission-track thermochronology by the external detector method, but poor yield, small grain-sizes, extremely few spontaneous tracks and no confined track lengths prevented acquisition of meaningful ages. As such, no apatite fission-track data are incorporated into our modeling effort.

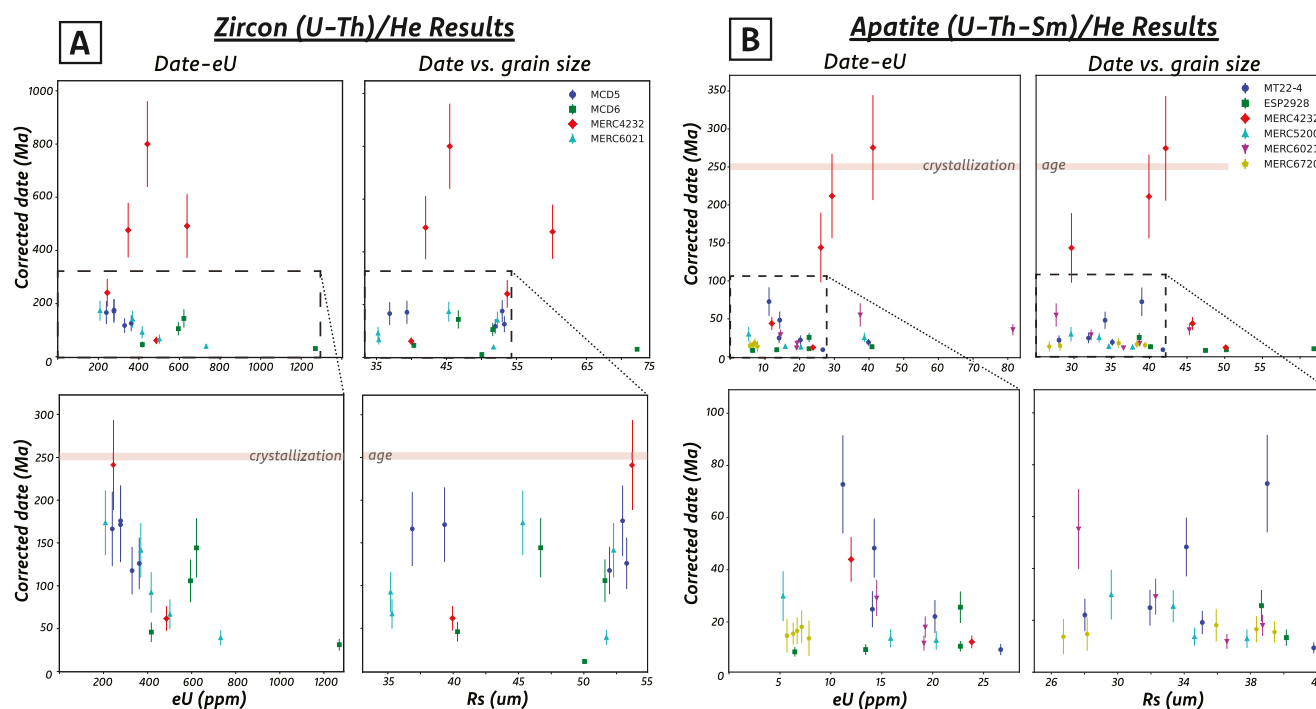


**Figure 4.** (a) Zircon and (b) apatite (U-Th-Sm)/He thermochronology results plotted against variables potentially responsible for dispersion. Left and right columns for each panel display date-eU and date-grain size comparisons, respectively.

### 3.2.2. Thermochronology Results

Five Durango apatites and four Fish Canyon Tuff zircons used as standards yielded average corrected dates of  $31.8 \pm 0.42$  and  $29.3 \pm 0.45$  Ma, respectively, within  $2\sigma$  error of published values (Reiners et al., 2004; Schmitz & Bowring, 2001). Analytical errors reflect the propagation of uncertainty from measurements of He, U, Th, and Sm and grain size. Uncertainties on the corrected (U-Th-Sm)/He dates are reported at  $2\sigma$  and include the propagated total analytical uncertainties (TAU) on the U, Th, and He measurements as well as an estimated uncertainty on the alpha-ejection correction, which was estimated to be 5%. Uncertainty calculation was completed with HeCalc software (Martin et al., 2023).

Zircon (U-Th)/He samples (ZHe) yield single grain dates between  $11.1 \pm 1.3$  and  $175.9 \pm 20.7$  Ma (Table 1), excluding the oldest dates from sample MERC4232, which are as old as ca. 800 Ma (Figure 4a). A negative relationship between ZHe date and effective uranium (eU) is observed, the latter of which is commonly used as a proxy for radiation damage (e.g., Guenther et al., 2013). The eU concentrations range from 208 to 1,270 ppm, with a relatively steep negative slope for grains with eU concentrations <750 ppm. Three grains with the highest eU values of 731, 1,270, and 4,930 ppm yield the youngest observed dates, forming a relatively flat tail characteristic of highly damaged (partially-reset) zircons (e.g., Orme et al., 2016; Ault et al., 2018; Figure 4a). No apparent trends between ZHe date and grain size (reported in this study as the radius of a sphere with a surface-area-to-volume ratio equivalent to that of the grain analyzed, or  $R_s$ ) are observed (Figure 4).

Apatite (U-Th-Sm)/He samples (AHe) single grain dates from the Mercedario transect have considerable intra-sample variation, ranging from  $8.5 \pm 0.9$  to  $275.4 \pm 34.5$  Ma (Figure 4; Table 2). Omitting dates from the most dispersed sample (MERC4232) results in an oldest date of  $72.7 \pm 9.4$  Ma. The two most reproducible data sets, with >4 single grain dates overlapping within error, are the topographically second lowest (ESP2928) and highest (MERC6720) samples. The highest sample from the summit of Cerro Mercedario yields five grains overlapping within  $2\sigma$  with a central age of  $15.7 \pm 2.9$  Ma. No obvious correlation between date-eU or date-grain size exists, except for sample MT22-4, which has negative and positive correlations, respectively (Figure 4b). The average apatite grain size ( $R_s$ ) across all samples is  $38.0 \mu\text{m}$ , with six grains having  $R_s < 30 \mu\text{m}$  (Figure 4b). Single grain dates from the Cordillera del Tigre sample range from  $14.2 \pm 1.9$  to  $41.1 \pm 4.3$  Ma, showing a positive correlation between He date and eU and no relationship between date and grain size (Table 2; Figure 7).

**Table 1**  
ZIRCON (U-Th)/He THERMOCHRONOLOGY DATA, Cerro Mercedario, Western Argentina

Sample name and aliquot	Length 1 (μm)	Width 1 (μm)	Length 2 (μm)	Width 2 (μm)	Np <sup>a</sup>	U (ng) <sup>b</sup>	U ± <sup>c</sup>	Th (ng) <sup>d</sup>	Th ± <sup>e</sup>	Rs (um) <sup>e</sup>	Mass (μg) <sup>f</sup>	<sup>4</sup> He (mmol/g) <sup>g</sup>	U (ppm) <sup>h</sup>	U ± <sup>i</sup>	Th (ppm) <sup>h</sup>	Th ± <sup>i</sup>	eU (ppm) <sup>j</sup>	Uncorr date (Ma)	1σ anal. ± (Ma)	F <sub>i</sub> comb <sup>k</sup>	Corrected date (Ma) <sup>k</sup>	± TAU + F <sub>i</sub> (Ma) 2σ <sup>l</sup>
Sample MCD5																						
Zr1	226	76	228	90	2	1.02	0.015	0.60	0.009	52.96	4.19	206.0	243.6	3.64	144.1	5.4	277.4	135.3	2.9	0.78	175.9	20.68
Zr2	224	79	223	89	2	1.44	0.021	0.72	0.010	53.27	4.45	192.4	324.3	3.36	161.4	7.1	362.2	97.1	2.1	0.78	126.1	15.08
Zr3	164	63	164	60	2	0.40	0.006	0.23	0.003	39.34	1.63	181.2	243.8	2.82	141.1	2.9	277.0	119.3	2.4	0.71	171.3	21.87
Zr4	150	69	154	50	2	0.35	0.005	0.24	0.004	36.87	1.69	148.1	206.1	2.85	143.2	3.3	239.8	112.7	2.6	0.69	166.4	21.75
Zr5	179	85	180	87	2	0.96	0.014	0.56	0.008	51.96	3.33	162.1	290.0	2.52	168.4	6.1	329.6	90.0	1.8	0.77	117.7	13.88
Sample MCD6																						
Zr1	317	128	319	100	2	11.83	0.176	7.42	0.106	72.24	10.69	178.1	1106.6	2.84	693.6	23.9	1269.6	25.8	0.5	0.83	31.3	3.45
Zr2	192	87	191	81	2	1.72	0.025	1.13	0.016	51.61	3.34	261.8	515.1	4.52	337.8	7.4	594.5	80.6	1.7	0.77	105.8	12.46
Zr3	174	65	175	61	2	0.63	0.010	0.51	0.007	40.33	1.81	72.9	350.6	1.09	281.7	5.8	416.8	32.2	0.6	0.72	46.0	5.70
Zr4	216	74	216	69	2	1.70	0.024	1.11	0.016	46.69	3.16	363.3	539.1	5.90	351.8	7.5	621.8	106.7	2.2	0.75	144.3	17.32
Zr5	182	88	183	75	2	9.91	0.141	6.32	0.092	50.05	2.31	224.0	4285.4	3.79	2735.1	59.4	4928.1	8.4	0.2	0.77	11.1	1.33
Sample MERC232																						
Zr1	137	75	137	60	2	0.48	0.007	0.53	0.008	39.95	1.25	113.6	385.7	2.09	425.3	9.5	485.7	43.0	0.6	0.72	61.8	7.20
Zr2	209	102	207	98	2	1.41	0.020	0.72	0.010	60.16	4.56	742.1	310.2	12.54	157.3	3.3	347.2	380.9	5.4	0.80	476.2	51.34
Zr3	181	92	178	86	2	0.69	0.010	0.56	0.009	53.68	3.37	250.3	205.3	4.19	165.2	3.7	244.1	186.0	2.6	0.78	241.0	26.19
Zr4	177	75	179	69	2	0.75	0.011	1.00	0.014	45.46	2.23	1488.4	336.7	25.03	447.0	9.9	441.7	591.9	6.6	0.75	799.9	80.78
Zr5	145	73	145	68	2	0.90	0.013	0.30	0.005	42.01	1.53	1268.1	591.0	20.15	196.4	4.3	637.2	355.2	4.6	0.72	492.0	60.03
Sample MERC6021																						
Zr1	213	82	213	81	2	1.42	0.020	0.87	0.012	52.27	4.41	218.8	322.7	3.53	196.7	7.0	369.0	108.3	1.4	0.78	141.4	15.95
Zr2	183	90	181	81	2	2.12	0.030	1.38	0.020	51.72	3.35	119.3	634.3	2.00	413.5	9.0	731.4	30.0	0.4	0.77	39.4	4.47
Zr3	380	74	374	59	2	0.76	0.011	0.91	0.013	45.32	4.69	144.6	162.8	2.67	194.1	4.6	208.4	126.6	1.5	0.75	173.5	18.87
Zr4	197	51	196	54	2	0.47	0.007	0.40	0.006	35.21	1.36	138.5	347.4	2.86	293.2	6.6	416.3	61.0	1.0	0.68	92.3	11.80
Zr5	159	61	162	50	2	0.43	0.006	0.33	0.005	35.32	1.01	120.7	424.7	2.55	325.2	7.4	501.1	44.2	0.8	0.68	66.8	8.63

<sup>a</sup>Np denotes the number of pyramidal terminations of the grain. <sup>b</sup>Total blank-corrected ng of <sup>238</sup>U. <sup>c</sup>Uncertainties on U, Th, and <sup>4</sup>He are reported as the 1σ standard error. <sup>d</sup>Total blank-corrected ng of <sup>232</sup>Th. <sup>e</sup>grain spherical radius, reported in this study as the radius of a sphere with a surface-area-to-volume ratio equivalent to that of the grain analyzed (Rs). <sup>f</sup>grain mass determined from measured grain dimensions. <sup>g</sup>Blank-corrected <sup>4</sup>He. <sup>h</sup>Concentration of each U and Th computed from the absolute amount of the measured isotopes. <sup>i</sup>eU is effective uranium concentration. <sup>j</sup>The combined alpha-ejection correction for the crystal calculated using equation A4 in Cooperdock et al. (2019). <sup>k</sup>The corrected (U-Th)/He date is calculated iteratively using the absolute values of He, U, Th, and the isotope specific FT corrections. <sup>l</sup>Uncertainty on the corrected (U-Th)/He date reported at 2σ and includes the propagated total analytical uncertainties (TAU) on the U, Th, and He measurements as well as an estimated uncertainty on the FT correction that is estimated to be 5%. Uncertainty calculation done with HeCalc (Martin et al., 2023).

**Table 2**  
**APATITE (U-Th-Sm)/He THERMOCRONOLOGY DATA, La Ramada Massif and Cordillera del Tigre, Western Argentina**

Sample name and aliquot	Length 1 (μm)	Width 1 (μm)	Length 2 (μm)	Width 2 (μm)	U (ng <sup>g</sup> ) ± b	Th (ng <sup>g</sup> ) ± b	Sm (ng <sup>g</sup> ) ± b	Rs (um) ± b	Mass (μg) ± b	<sup>4</sup> He (mmol/g) ± b	U (ppm) ± b	Th (ppm) ± b	Sm (ppm) ± b	eU (ppm) ± b	Uncon. date (Ma) ±	Is err. anal. ± (Ma)	Pt comb.	Corrected date (Ma) ±	± TAU + Ft (Ma) ± 2σ
Sample MT22-4																			
Ap1	127	68	125	65	0.02 ± 2.9E-04	0.10 ± 1.4E-03	1.07 ± 1.6E-02	35 ± 1.23	2.5 ± 0.02	18.21 ± 0.26	89.98 ± 1.28	961.57 ± 14.67	39.9 ± 5.98	11.35 ± 11.35	0.14 ± 0.14	0.68 ± 0.68	19.18 ± 19.18	2.25 ± 2.25	
Ap2	93	52	96	50	0.00 ± 7.4E-05	0.02 ± 2.3E-04	0.24 ± 3.6E-03	28 ± 0.46	1.1 ± 0.03	9.35 ± 0.15	32.13 ± 0.46	487.47 ± 7.40	20.2 ± 3.03	11.33 ± 11.33	0.33 ± 0.33	0.58 ± 0.58	22.06 ± 22.06	3.15 ± 3.15	
Ap3	107	61	106	57	0.00 ± 7.6E-05	0.02 ± 2.4E-04	0.31 ± 4.6E-03	34 ± 0.65	1.7 ± 0.02	5.76 ± 0.10	20.91 ± 0.32	414.04 ± 6.28	14.3 ± 2.14	28.54 ± 28.54	0.50 ± 0.50	0.65 ± 0.65	48.30 ± 48.30	5.67 ± 5.67	
Ap4	94	61	103	65	0.01 ± 9.5E-05	0.01 ± 1.3E-04	0.27 ± 4.0E-03	32 ± 0.69	0.9 ± 0.02	8.10 ± 0.12	11.33 ± 0.17	340.52 ± 5.08	14.1 ± 2.11	14.29 ± 14.29	0.40 ± 0.40	0.60 ± 0.60	24.86 ± 24.86	3.47 ± 3.47	
Ap5	160	65	159	72	0.01 ± 1.3E-04	0.00 ± 6.4E-05	0.55 ± 8.3E-03	39 ± 1.06	1.7 ± 0.03	5.53 ± 0.09	2.78 ± 0.04	368.91 ± 5.50	11.2 ± 1.68	47.79 ± 47.79	0.98 ± 0.98	0.65 ± 0.65	72.74 ± 72.74	9.40 ± 9.40	
Ap6	112	73	105	74	0.01 ± 2.7E-04	0.05 ± 7.1E-04	0.65 ± 9.7E-03	42 ± 1.02	0.7 ± 0.01	10.44 ± 0.23	41.43 ± 0.60	542.73 ± 8.11	26.7 ± 4.00	6.12 ± 6.12	0.15 ± 0.15	0.71 ± 0.71	9.38 ± 9.38	1.07 ± 1.07	
Sample ESP2928																			
Ap1	155	75	155	68	0.03 ± 3.9E-04	0.05 ± 7.3E-04	0.24 ± 4.1E-03	39 ± 1.70	2.1 ± 0.02	16.18 ± 0.24	31.71 ± 0.46	150.21 ± 2.57	22.7 ± 3.41	16.12 ± 16.12	0.22 ± 0.22	0.67 ± 0.67	25.63 ± 25.63	3.03 ± 3.03	
Ap2	164	94	164	87	0.01 ± 1.3E-04	0.03 ± 3.7E-04	0.98 ± 1.5E-02	47 ± 3.01	0.2 ± 0.00	3.31 ± 0.05	9.34 ± 0.14	363.13 ± 5.44	6.5 ± 0.97	5.98 ± 5.98	0.16 ± 0.16	0.73 ± 0.73	8.51 ± 8.51	0.91 ± 0.91	
Ap3	249	94	247	84	0.03 ± 4.6E-04	0.05 ± 7.8E-04	1.20 ± 1.8E-02	50 ± 3.72	0.4 ± 0.01	7.90 ± 0.12	13.69 ± 0.20	300.63 ± 4.51	13.4 ± 2.01	6.68 ± 6.68	0.14 ± 0.14	0.74 ± 0.74	9.37 ± 9.37	1.03 ± 1.03	
Ap4	154	72	156	63	0.04 ± 6.5E-04	0.07 ± 1.0E-03	0.51 ± 7.6E-03	40 ± 1.52	2.0 ± 0.02	30.17 ± 0.46	49.43 ± 0.71	354.67 ± 5.32	40.9 ± 6.13	8.57 ± 8.57	0.12 ± 0.12	0.68 ± 0.68	13.32 ± 13.32	1.58 ± 1.58	
Ap5	268	104	276	102	0.06 ± 8.8E-04	0.16 ± 2.2E-03	1.39 ± 2.1E-02	62 ± 4.61	0.8 ± 0.00	10.59 ± 0.15	27.08 ± 0.39	239.27 ± 3.54	22.7 ± 3.41	8.08 ± 8.08	0.10 ± 0.10	0.79 ± 0.79	10.67 ± 10.67	1.01 ± 1.01	
Sample MERC4232																			
Ap1	146	55	148	47	0.02 ± 2.7E-04	0.01 ± 1.3E-04	0.10 ± 1.6E-03	30 ± 0.77	11.1 ± 0.04	23.27 ± 0.35	10.52 ± 0.17	132.00 ± 2.12	26.1 ± 3.92	78.89 ± 78.89	1.09 ± 1.09	0.56 ± 0.56	143.89 ± 143.89	22.96 ± 22.96	
Ap2	144	77	143	76	0.05 ± 7.2E-04	0.03 ± 4.7E-04	0.34 ± 5.7E-03	42 ± 1.45	35.0 ± 0.06	29.84 ± 0.43	19.49 ± 0.28	204.95 ± 3.40	41.1 ± 6.17	184.24 ± 184.24	2.29 ± 2.29	0.68 ± 0.68	275.45 ± 275.45	34.56 ± 34.56	
Ap3	191	80	191	73	0.01 ± 1.7E-04	0.03 ± 3.9E-04	1.03 ± 1.5E-02	46 ± 1.67	1.2 ± 0.01	3.96 ± 0.07	11.94 ± 0.17	458.34 ± 6.87	12.0 ± 1.80	30.45 ± 30.45	0.42 ± 0.42	0.73 ± 0.73	43.98 ± 43.98	4.29 ± 4.29	
Ap4	159	78	158	63	0.03 ± 4.5E-04	0.02 ± 2.5E-04	0.27 ± 4.3E-03	40 ± 1.25	16.8 ± 0.03	19.59 ± 0.28	10.83 ± 0.16	170.08 ± 2.70	29.3 ± 4.40	138.15 ± 138.15	1.77 ± 1.77	0.66 ± 0.66	211.72 ± 211.72	27.75 ± 27.75	
Ap6	137	85	137	84	0.02 ± 2.6E-04	0.06 ± 9.0E-04	1.09 ± 1.6E-02	50 ± 1.58	0.8 ± 0.01	8.97 ± 0.13	32.20 ± 0.46	553.84 ± 8.34	23.8 ± 3.58	8.71 ± 8.71	0.13 ± 0.13	0.75 ± 0.75	12.31 ± 12.31	1.22 ± 1.22	
Sample MERC5200																			
Ap1	244	62	246	51	0.03 ± 4.0E-04	0.07 ± 1.0E-03	0.63 ± 9.7E-03	33 ± 1.23	2.3 ± 0.01	17.74 ± 0.25	45.06 ± 0.64	403.38 ± 6.17	38.7 ± 5.80	14.68 ± 14.68	0.18 ± 0.18	0.63 ± 0.63	25.39 ± 25.39	3.11 ± 3.11	
Ap2	113	58	116	52	0.00 ± 5.8E-05	0.01 ± 1.6E-04	0.26 ± 4.2E-03	30 ± 1.27	0.7 ± 0.04	4.41 ± 0.08	15.06 ± 0.23	371.81 ± 6.00	5.3 ± 0.80	16.21 ± 16.21	0.84 ± 0.84	0.60 ± 0.60	29.89 ± 29.89	4.78 ± 4.78	
Ap3	120	66	120	60	0.01 ± 1.4E-04	0.02 ± 2.7E-04	0.20 ± 3.2E-03	38 ± 0.67	0.6 ± 0.02	8.79 ± 0.14	18.84 ± 0.28	213.06 ± 3.32	20.3 ± 3.05	8.04 ± 8.04	0.32 ± 0.32	0.66 ± 0.66	12.90 ± 12.90	1.79 ± 1.79	
Ap4	103	63	104	57	0.01 ± 6.6E-05	0.02 ± 2.9E-04	0.27 ± 4.2E-03	35 ± 0.77	0.7 ± 0.02	8.55 ± 0.13	25.68 ± 0.38	363.59 ± 5.62	15.9 ± 2.38	1.8 ± 1.8	0.24 ± 0.24	0.65 ± 0.65	13.70 ± 13.70	1.76 ± 1.76	

**Table 2**  
*Continued*

Sample name and aliquot	Length 1 (μm)	Width 1 (μm)	Length 2 (μm)	Width 2 (μm)	U (ng) <sup>a</sup>	Th (ng) <sup>c</sup>	Sm (ng) <sup>d</sup>	Rs (um) <sup>e</sup>	Mass (μg) <sup>f</sup>	<sup>4</sup> He (nmol/g) <sup>g</sup>	U (ppm) <sup>h</sup>	Th (ppm) <sup>h</sup>	Sm (ppm) <sup>h</sup>	eU (ppm) <sup>j</sup>	Uncorr. date (Ma)	Is er anal. ± (Ma)	Ft comb <sup>k</sup>	Corrected date (Ma) <sup>k</sup>	± TAU + Ft (Ma) 2 $\sigma$ <sup>l</sup>								
Sample MERC6021																											
Ap1	174	79	174	81	0.07	9.9E-04	0.27	3.9E-03	1.88	2.9E-02	45	1.74	7.9	0.03	30.83	0.44	120.56	1.72	837.36	12.84	81.5	12.22	24.11	0.26	0.73	35.79	3.69
Ap2	190	51	189	43	0.01	1.6E-04	0.08	1.1E-03	1.03	1.6E-02	28	0.89	5.3	0.02	12.53	0.18	89.67	1.29	1,217.78	18.62	37.5	5.62	27.70	0.30	0.63	55.19	7.70
Ap4	138	70	139	62	0.01	1.4E-04	0.03	4.0E-04	0.95	1.5E-02	39	1.03	0.9	0.02	7.36	0.12	22.81	0.33	792.58	12.27	19.3	2.89	11.56	0.27	0.68	18.03	2.02
Ap5	118	65	120	60	0.01	1.1E-04	0.02	2.6E-04	0.80	1.3E-02	37	0.77	0.5	0.01	7.32	0.12	19.00	0.28	844.25	13.35	19.1	2.87	7.45	0.22	0.66	11.87	1.43
Ap6	115	65	114	58	0.00	7.2E-05	0.01	1.7E-04	0.61	9.4E-03	32	0.69	0.8	0.02	5.11	0.08	13.20	0.19	711.47	10.96	14.5	2.17	17.19	0.40	0.62	29.14	3.46
Sample MERC6720																											
Ap1	176	59	178	59	0.00	5.1E-05	0.01	1.6E-04	0.24	3.8E-03	38	0.90	0.2	0.01	1.94	0.04	8.58	0.13	193.64	3.04	6.7	1.00	10.47	0.59	0.69	16.60	2.55
Ap2	246	45	246	42	0.00	5.3E-05	0.01	9.5E-05	0.11	1.8E-03	28	0.82	0.2	0.02	2.89	0.06	6.76	0.10	120.59	1.98	5.7	0.85	7.65	0.67	0.57	14.72	3.23
Ap4	140	65	143	56	0.00	5.3E-05	0.01	1.4E-04	0.18	2.9E-03	36	0.76	0.3	0.02	2.39	0.05	8.61	0.14	176.26	2.81	7.1	1.07	11.04	0.74	0.67	18.14	3.14
Ap5	134	79	133	56	0.00	7.3E-05	0.01	1.9E-04	0.32	5.1E-03	39	1.40	0.3	0.01	3.53	0.06	10.65	0.16	262.65	4.22	6.3	0.94	9.94	0.44	0.69	15.48	2.10
Ap6	133	53	132	42	0.00	6.3E-05	0.01	1.2E-04	0.13	2.0E-03	27	0.77	0.3	0.04	5.96	0.10	13.09	0.20	215.19	3.35	7.8	1.18	6.82	0.70	0.54	13.69	3.41
Sample CDT2-2,745																											
Ap1	73	69	73	61	0.003	5.0E-05	0.01	1.7E-04	0.30	4.4E-03	42	0.51	1.3	0.02	4.28	0.08	17.74	0.28	485.06	7.14	13.0	1.95	27.32	0.50	0.72	41.14	4.30
Ap2	171	60	174	64	0.004	7.4E-05	0.02	3.7E-04	0.66	1.0E-02	38	1.17	0.4	0.02	3.24	0.05	18.47	0.27	490.83	7.64	11.3	1.70	9.00	0.38	0.71	14.22	1.91
Ap3	192	59	193	50	0.003	5.4E-05	0.02	2.5E-04	0.46	6.9E-03	35	0.89	0.5	0.02	2.66	0.05	14.36	0.22	405.37	6.03	10.2	1.53	12.89	0.68	0.68	21.20	3.20
Ap4	112	54	113	55	0.002	6.4E-05	0.01	1.8E-04	0.29	4.3E-03	32	0.46	0.8	0.03	3.19	0.09	17.52	0.27	424.87	6.41	13.7	2.05	19.27	0.79	0.65	33.79	4.79
Ap5	101	53	100	46	0.002	6.2E-05	0.01	2.1E-04	0.27	4.0E-03	27	0.42	0.9	0.05	4.07	0.13	25.51	0.42	556.58	8.29	14.6	2.19	16.30	0.85	0.61	32.05	5.38

<sup>a</sup>Total blank-corrected ng of <sup>238</sup>U. <sup>b</sup>Uncertainties on U, Th, Sm, and <sup>4</sup>He are reported as the 1 $\sigma$  standard error. <sup>c</sup>Total blank-corrected ng of <sup>232</sup>Th. <sup>d</sup>Total blank-corrected ng of <sup>147</sup>Sm. <sup>e</sup>grain spherical radius, reported in this study as the radius of a sphere with a surface-area-to-volume ratio equivalent to that of the grain analyzed (Rs). <sup>f</sup>grain mass determined from measured grain dimensions. <sup>g</sup>Blank-corrected <sup>4</sup>He. <sup>h</sup>Concentration of each element (U, Th, and Sm) computed from the absolute amount of the measured isotopes (where <sup>147</sup>Sm is 0.15 of the total Sm reported here). <sup>i</sup>eU is effective uranium concentration. <sup>j</sup>The combined alpha-ejection correction for the crystal calculated using equation A4 in Cooperdock et al. (2019). <sup>k</sup>The corrected (U-Th-Sm)/He date is calculated iteratively using the absolute values of He, U, Th, Sm, and the isotope specific FT corrections. <sup>l</sup>Uncertainty on the corrected (U-Th)/He date reported at 2 $\sigma$  and includes the propagated total analytical uncertainties (TAU) on the U, Th, Sm, and He measurements as well as an estimated uncertainty on the FT correction that is estimated to be 5%. Uncertainty calculation done with HeCalc (Martin et al., 2023).

### 3.2.3. Interpretation of Date-Elevation Relationships

Date-elevation relationships from Cerro Mercedario display dispersion in our data set but reveal trends that facilitate our data filtration approach and the interpretation of cooling signals (Figure 5). ZHe dates from our lowest samples (2–3 km asl) are dispersed but approach the crystallization age of host rocks with increasing elevation (Figure 5b). These dates are interpreted to represent partial resetting of the ZHe system by residence of the lowest samples within the ZHe partial retention zone (PRZ) at the onset of Andean exhumation. An alternative explanation is that samples cooled to near surface temperature following crystallization and were reheated by sediment and/or thrust sheet burial from the impinging thrust belt to the west. By extrapolating the average dip from the west-dipping panel of Triassic strata (Figure 2b) across the Cordon del Espinacito basement block, we calculate an approximate true overburden thickness of ~5.8 km for our lowest elevation sample. Assuming that some thickness of Jurassic and younger strata was eroded from above this sample, the combined thickness is adequate to position these samples in or near the ZHe PRZ prior to Miocene exhumation. It also implies that little to no burial by younger synorogenic sediments is required, as any significant added thickness would have probably heated samples above the ZHe PRZ.

The two highest ZHe samples were analyzed to test the hypothesis that the whole transect was uplifted and exhumed along the Espinacito fault system, with the Santa Cruz fault representing a relatively minor, perhaps out-of-sequence thrust fault. If this hypothesis is correct, expected ZHe dates would approach and/or overlap the Choiyoi crystallization age since samples would be progressively farther from the ZHe PRZ interpreted for the lower sample group. Such a straight-forward interpretation for the high ZHe samples is complicated by high dispersion, likely caused by factors other than prolonged residence in the ZHe PRZ as demonstrated in subsequent modeling efforts. If ZHe dispersion in the high sample group is interpreted to be the result of residence in the ZHe PRZ, this requires the Santa Cruz hanging wall to have experienced a magnitude of erosion similar to that in the Cordon del Espinacito (removal of at least 6 km of material assuming a typical geothermal gradient of 25°C/km).

Comparable trends between ZHe date and elevation have been used to determine the timing and magnitude of exhumation in southern portions of the Frontal Cordillera (Riesner et al., 2019). These authors interpreted their lowest sample to have resided in or near the ZHe PRZ prior to Cenozoic exhumation, and their interpretation of rapid cooling onset relies on their youngest single ZHe date from this sample. In contrast, their highest ZHe sample, collected at ~4.3 km asl, produced dates overlapping with the crystallization age of the host rock, suggesting no resetting of the ZHe system. A notable aspect of our ZHe data set is that the single-grain dispersion observed in MERC6021 is similar to what is observed in the lowest sample of Riesner et al. (2019), even though our sample was collected approximately 4 km higher in elevation.

The youngest AHe date(s) increase with elevation (Figure 5c). The most reproducible low elevation sample (ESP2928) produced four single grains overlapping within  $2\sigma$  with a weighted mean age of  $10.47 \pm 1.13$  Ma. Increasing date with elevation is observed when considering the youngest date from sample MERC4232, the two youngest dates from MERC5200, the two youngest dates from MERC6021, and all five dates from the highest sample. This trend is not noticeably disrupted across the Santa Cruz fault and the Santa Cruz hanging wall records older dates (Figure 5c). A linear age-elevation trend suggests continuous exhumation from at least 18–14 Ma to 11.5–9.5 Ma; however, we hesitate to interpret samples above and below the Santa Cruz fault as a single group for reasons described in the following sections. It is noteworthy that an uncertainty-weighted regression of the youngest average AHe dates across all samples yields an apparent exhumation rate of ~0.3–0.4 mm/yr (~400 m/Myr) (Figure 5c). This rate is comparable to rates determined for the Frontal Cordillera from existing data sets (Lossada et al., 2017; Riesner et al., 2019), giving us additional confidence that our youngest AHe dates are capturing a regional cooling signature.

### 3.2.4. Handling Complex He Data Prior to Modeling

Similar to existing (U-Th-Sm)/He data sets from the Frontal Cordillera province (e.g., Hoke et al., 2014), our data are complex and require an inspection of possible causes of single-grain dispersion. Numerous complicating factors, such as U- and Th-rich (micro)inclusions, fluid inclusions, variation in crystal size, alpha-particle ejection correction, zonation and He implantation can contribute to date dispersion (e.g., Farley et al., 1996; Fitzgerald et al., 2006). Poor apatite yield and quality is characteristic of the Choiyoi Group and grains are typically small (Hoke et al., 2014; Mackaman-Lofland et al., 2020). Our approach to identifying possible causes of dispersion and subsequent interpretations is guided by the review from He et al. (2021). These authors show that for rapidly

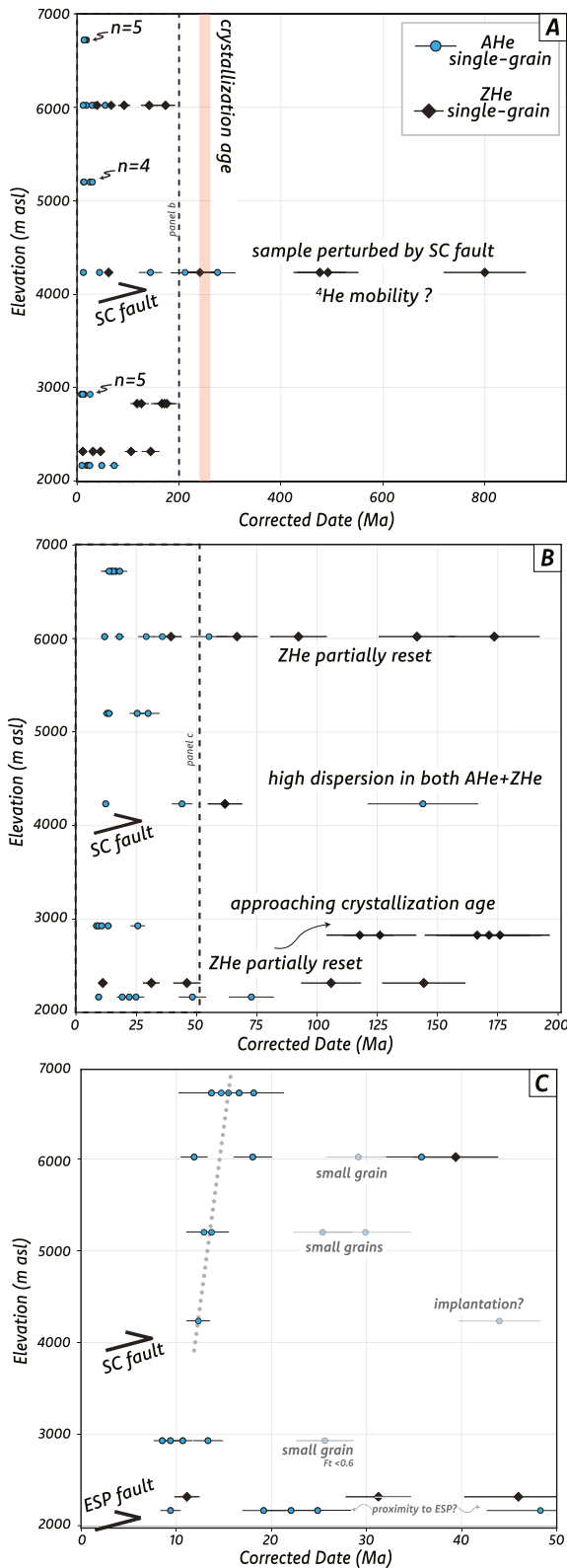


**Figure 5.** Helium date versus elevation plots showing intra-sample single-grain dispersion and trends with increasing elevation. Panels A, B, and C zoom in toward progressively younger dates (maximum x-axis values of 1,000, 200, and 50 Ma, respectively).

cooled samples where dispersion caused by variable eU and grain size is minimized, probable sources of dispersion (such as helium trapping, damage-modified diffusivity, etc.) tend to cause anomalously old helium dates. We interpret a significant degree of skewing toward old AHe dates in our data set. Most outlying grains that do not fit the positive date-elevation correlation are relatively small and fragmented (Data Set S1).

Overdispersion in two samples may be related to fault proximity. Sample MERC4232 was collected in the proximal hanging wall above the Santa Cruz fault and shows the greatest degree of single-grain dispersion in both the ZHe and AHe systems (Figures 4 and 5). This dispersion is interpreted to be the result of He implantation, perhaps related to mobility of  $^4\text{He}$  due to the hydrothermal activity (*sensu* Milesi et al., 2019) that is observed in the Santa Cruz fault zone (e.g., Figures 3d and 3e). The sample with next highest degree of dispersion (MT22-4) was collected most proximal to the Espinacito fault and may have been affected by similar helium perturbations related to faulting, although our preferred interpretation is that ZHe date dispersion in this sample is due to residence in the ZHe PRZ. The apatite quality in this sample was poor, and grain images reveal fragmented grains that are likely producing dispersed AHe dates due to a combination of the variables described above. Characteristics of each grain analyzed in this study are detailed in the Supporting Information (Data Set S1).

### 3.3. Modeling of Thermochronometric Data

#### 3.3.1. Inverse and Forward Modeling of Mercedario Vertical Transect

Thermal history modeling of AHe and ZHe data was performed with the QTQt software (version 5.8.0). QTQt applies a Bayesian trans-dimensional approach to Markov Chain Monte Carlo statistics (Gallagher, 2012) to produce a cooling evolution of the sample that predicts the measured data by applying a user specified He diffusion model (this study utilizes the Flowers et al. (2009) and Guenther et al. (2013) diffusion models for AHe and ZHe, respectively). Given the large degree of vertical separation between our highest and lowest samples, we utilize QTQt's ability to jointly model multiple samples with a known vertical relationship. This is a powerful approach in that it (a) increases the likelihood of recovering a better resolved thermal history, and (b) enables us to explore the effects of each sample on the modeled thermal history and further identify outlying single grains that are incompatible with geologically plausible cooling paths (e.g., Abbey et al., 2023).

We began modeling efforts by conducting vertical profile sensitivity tests following the workflow outlined in Abbey et al. (2023). Detailed model inputs, outputs, decisions made, and interpretations for sensitivity tests and subsequent modeling can be found in the Supporting Information (Figure S1 in Supporting Information S1 and Data Sets S2 and S3). Sensitivity testing is an effective approach to better understand the effect of each sample on the resolved thermal history and enables identification of potential outlying grains that have dates inconsistent with geologically plausible cooling histories. Experimentally removing samples from our modeled profile moderately changes the timing of Cenozoic cooling, but the results consistently demonstrate a better observed versus predicted match in younger grains (Figure S1 in Supporting Information S1). We therefore use the sensitivity test outputs in tandem with other potential controls on anomalously old helium dates, such as grain size, to refine our model inputs and resolve exhumation-related cooling signatures.

Following sensitivity tests and omission of anomalously old dates (interpreted to be the result of implantation, crystal size, or a combination of other factors which skew grains toward older values), we jointly modeled AHe data for the entire vertical profile, disregarding the Santa Cruz fault. The resulting time-temperature paths show rapid cooling between ca. 19.5 and 16 Ma and produce output AHe dates that are in general agreement with our observed data (Figure 6a). Modeled paths place the lowest two samples at 150–180°C, consistent with the interpretation that the samples resided within the ZHe PRZ prior to the onset of rapid exhumation. Sample MERC6021 maintains a temperature below the ZHe PRZ, suggesting that the dispersion in single grain ZHe dates may be caused by something other than residence within the ZHe PRZ. Following this preliminary approach, we modeled AHe data in two groups above and below the Santa Cruz fault. The high and low sample groups show cooling between ca. 23 and 17.5 Ma, and 12.5 and 8.5 Ma, respectively (Figure 6b). The wide 95% credible path intervals prior to rapid exhumation in our expected time-temperature outputs demonstrate that separately grouped AHe data are not capable of resolving the earlier portion of the thermal history (Figure 6b). Given the horizontal distance and presence of the Santa Cruz fault between samples (Figures 1 and 3a), modeling the hanging wall sample groups separately is preferred for interpreting the timing of uplift and exhumation.

Attempts to jointly invert ZHe and AHe dates were inconclusive, with QTQt unable to reproduce the observed dates across samples with geologically meaningful time-temperature paths. To investigate possible causes of the discrepancy between data sets and explore the apparent negative correlation between ZHe date and effective uranium (eU), we implemented a series of forward models using the damage and annealing model (DAAM) script of Guenther et al. (2013), which incorporates a He diffusion model and alpha ejection correction and is used to assess the validity of potential time-temperature paths for producing an observed date-eU trend (<https://github.com/wrguenther/DAAM>). A significant finding from this experiment is that there are no time-temperature paths that can reproduce the negative date-eU relationships (Figure S2 in Supporting Information S1), suggesting the apparent negative correlation is the result of factors outside the commonly cited radiation-damage-diminished retention of daughter product (e.g., Härtel et al., 2022). Specifically, we find that assuming a Choiyoi crystallization age of ca. 250 Ma, there is insufficient time (regardless of holding temperature) prior to uplift for adequate radiation damage to accumulate. This is especially relevant for MERC6021, the sample with the most pronounced negative relationship between date and eU (Figure 4a). Samples from the hanging wall of the Espinacito fault display both negative and positive relationships across the same range of eU (MCD5 and MCD6, respectively; Figure 4a and Figure S2 in Supporting Information S1), making it impossible to reproduce the expected curves with a shared thermal history. Despite modeling difficulties encountered due to ZHe dispersion, we maintain the interpretation that low samples in the proximal hanging wall of the Espinacito fault experienced residence in the ZHe PRZ based on the modern geology, scale of the fault, and ZHe dates approaching the Choiyoi crystallization age with increasing elevation (Figure 5).

An alternative explanation for the ZHe dispersion in the Espanicito hanging wall involves (a) dispersion in lower sample MCD6 due to fault-related or other perturbation(s) of the system, and (b) a captured Middle- to Late-Jurassic cooling signature in the more internally consistent MCD5, potentially related to normal faulting in the northern Neuquén basin (e.g., Ramos et al., 1996). Single-sample modeling of MCD5 enabled the identification of one problematic grain (the youngest grain in the sample, Zr5) which was preventing the model from finding reasonable time-temperature paths. An inversion containing the other four grains reveals a relatively well-constrained cooling signature at ca. 150 Ma (Figure S3 in Supporting Information S1). We emphasize two points regardless of the preferred cooling history contained in the ZHe data: (a) erosion related to the main phase of Andean mountain building at this latitude is insufficient to expose fully reset ZHe dates, and (b) dispersion in the ZHe system does not affect our preferred interpretation for the timing of thrusting recorded by AHe data between ca. 23 and 17.5 Ma and 12.5 and 8.5 Ma in the Santa Cruz and Espinacito hanging walls, respectively.

Our data sets, particularly the ZHe results, highlight a potential complicating factor for the interpretation of thermochronology data in this region. We have demonstrated that the large degree of dispersion in the ZHe data cannot be reconciled with plausible time-temperature paths; as such, the youngest single grains from bedrock (e.g., Riesner et al., 2019) or detrital grains from the adjacent basin record (e.g., Fosdick et al., 2024) may result in erroneous interpretations for the timing of shortening-related exhumation in the Frontal Cordillera. There are Eocene-Miocene ZHe dates in our data set from Frontal Cordillera bedrock that are seemingly controlled by factors outside of rock uplift and exhumation related to Andean mountain building. The intimate linkage between cooling, exhumation, hydrothermal heating, and widespread porphyry-epithermal deposits (e.g., El Pachón and

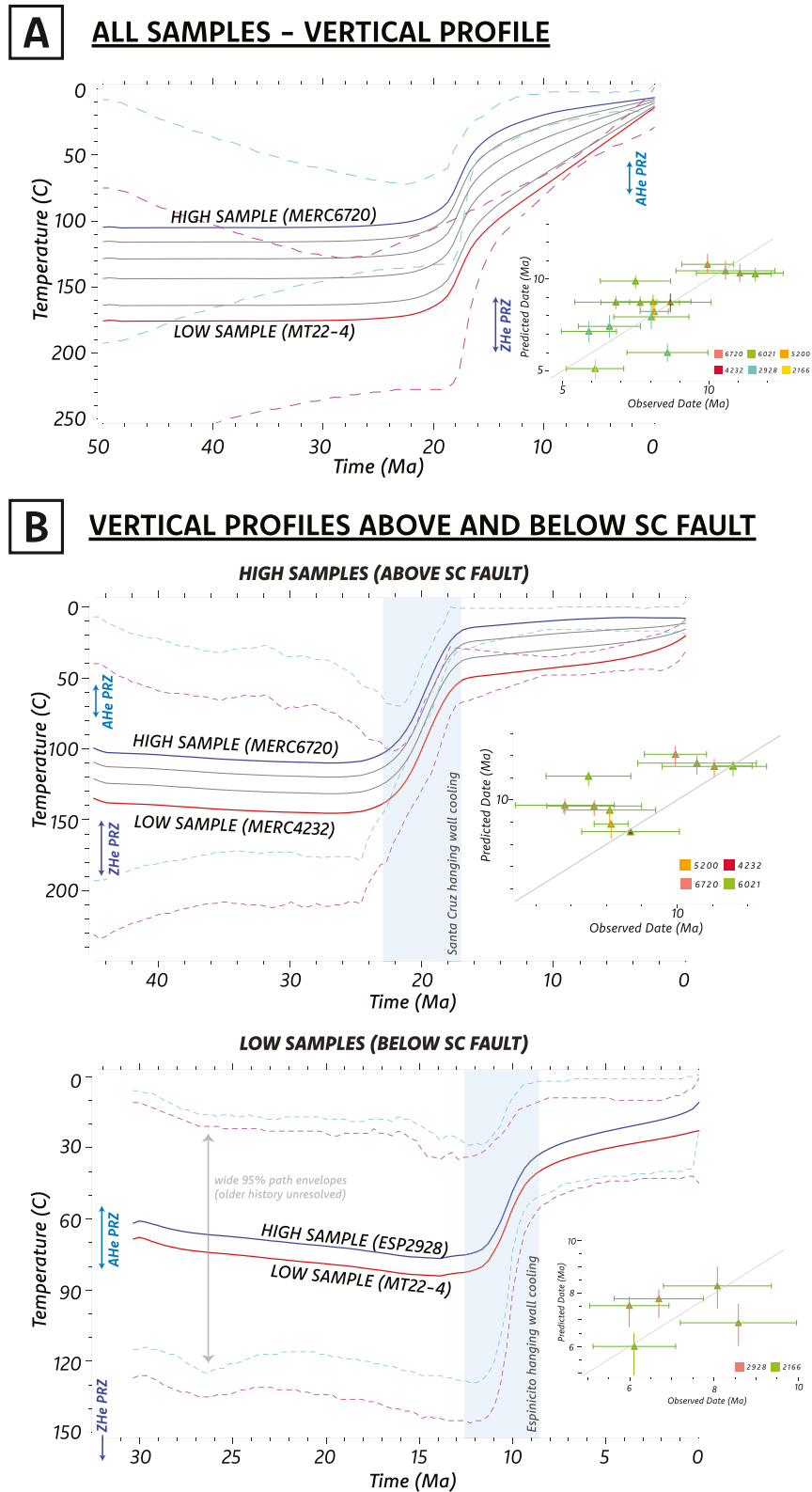


Figure 6.

Pelambres) may contribute to some of the observed dispersion in low-temperature thermochronology data sets from this region (e.g., Maydagán et al., 2014, 2020; Milesi et al., 2019, 2020) and should be considered carefully.

### 3.3.2. Thermal History Modeling for the Cordillera del Tigre

Our modeling approach for the partially reset Cordillera del Tigre (CDT) sample is guided by recent findings from the westward adjacent Manantiales Basin. We first implement a forward modeling approach for our Cordillera del Tigre AHe sample that uses the apatite radiation damage and annealing model (ARDAAM) of Flowers et al. (2009). Three plausible thermal histories, all beginning at the Choiyoi crystallization age of ca. 250 Ma, are tested, including: (a) protracted residence below the AHe closure temperature followed by moderate Oligo-Miocene foredeep burial (5.5°C/Ma) and rapid late Miocene cooling (35°C/Ma); (b) “early” CDT cooling between 22 and 17 Ma at 10°C/Ma; and (c) protracted residence in the upper AHe PRZ followed by the same late Miocene cooling as in scenario one (Figure 7c). Scenarios one and two produce earlier inflection points in the date-eU correlation and predict AHe dates older than are observed. In contrast, scenario three predicts a date-eU correlation that overlaps within  $2\sigma$  for four of the five observed dates (Figure 7c). We inverted the AHe data from CDT with both QTQt and the HeFTy software (Ketcham, 2024) and present an output from the latter as the ability to identify “acceptable” and “good” fit paths is valuable in the context of our adjacent forward models (Figure 7). Inverse models are constrained with one initial temperature window between 0° and 200°C at 240–260 Ma and a final present-day temperature of 20°C. Modeled t-T paths with an episodic randomizing style were run until 50 good fit paths were reached. To more fully allow the data to determine a variety of possible t-T histories, the segment between the initial constraint and present-day temperature was halved four times (i.e., four nodal points allowing changes in slope). The merit values for “good” and “acceptable” fits are 0.5 and 0.05, respectively. Inverse modeling in HeFTy enabled the identification of a single grain (Ap2) which prevented the software from finding any good fit paths; this is the youngest grain in our sample and is the only grain in our forward modeling with  $2\sigma$  uncertainty not overlapping with the predicted date-eU curve (Figure 7c). Removal of this grain enabled HeFTy to find good fit paths, which are generally consistent with the best-fit path from our forward modeling (Figures 7c and 7d). Importantly, good fit paths require sustained residence in the AHe PRZ from Choiyoi crystallization until Oligo-Miocene time, with the best fit path showing cooling ca. 11–8 Ma (Figure 7d). Other good fit paths between ca. 24–20 Ma cannot be discounted with available data and may capture an earlier pulse of cooling in the Early Miocene.

Considering forward and inverse models together, the data most convincingly capture Late Miocene cooling (Figure 7); however, partially reset AHe dates from the Cordillera del Tigre must be considered in the structural context of the sample and alongside recent work from the Manantiales basin. The Manantiales basin contains more than 4 km of Cenozoic deposits with reset (mainly  $\leq 15$  Ma) AHe ages in even the central to upper levels of the basin fill (Jordan et al., 1996; Mackaman-Lofland et al., 2020). By contrast, older AHe dates from the Cordillera del Tigre indicate that overlying deposits were of insufficient thickness to completely reset the AHe system (i.e.,  $<2.5$  km assuming a 25°C/km geothermal gradient). Therefore, the Cordillera del Tigre was likely initially elevated prior to or during deposition of Miocene basin fill, consistent with reported evidence for wedge-top deposition in  $\leq 18$  Ma strata of the Manantiales basin (Ronemus et al., 2024). Although the forward model test of this thermal history (scenario two) produces AHe dates older than observed (Figure 7c), our sample was collected from relatively low elevation (2,800 m asl) and earlier cooling signatures (if preserved) would be recorded higher in the CDT, which reaches elevations  $>5,500$  m asl (Figure 2).

Our thermal history models indicate that cooling ca. 11–9 Ma can best reproduce observed AHe date-eU trends (Figure 7c). This cooling timing is consistent with the termination of sedimentation and inception of cooling in the Manantiales basin (Mackaman-Lofland et al., 2020; Ronemus et al., 2024) and likely indicates a second phase of uplift of the Cordillera del Tigre. Collectively, an initial phase of uplift of the Cordillera del Tigre during deposition of the Manantiales basin fill (ca. 18–16 Ma) in combination with a second phase of Late Miocene uplift

**Figure 6.** (a) QTQt expected time-temperature path for entire vertical profile displaying cooling of all samples between ca. 20 and 18 Ma. (b) Modeling the transect in two samples groups above and below the Santa Cruz fault (SC fault). For both (a) and (b), the uncorrected observed versus predicted date plots are shown as insets, with triangle color corresponding to sample ID. All paths originate in the middle of a single constraint box, placed arbitrarily due to the inability of apatite (U-Th-Sm)/He data to resolve the early portions of the time-temperature history. This is graphically represented by dashed lines indicating broad 95% credible intervals before 20 Ma. AHe PRZ—nominal closure temperature for the apatite (U-Th-Sm)/He system; ZHe PRZ—nominal closure temperature for the zircon (U-Th)/He system. All model inputs and choices are detailed in Howlett et al. (2024).

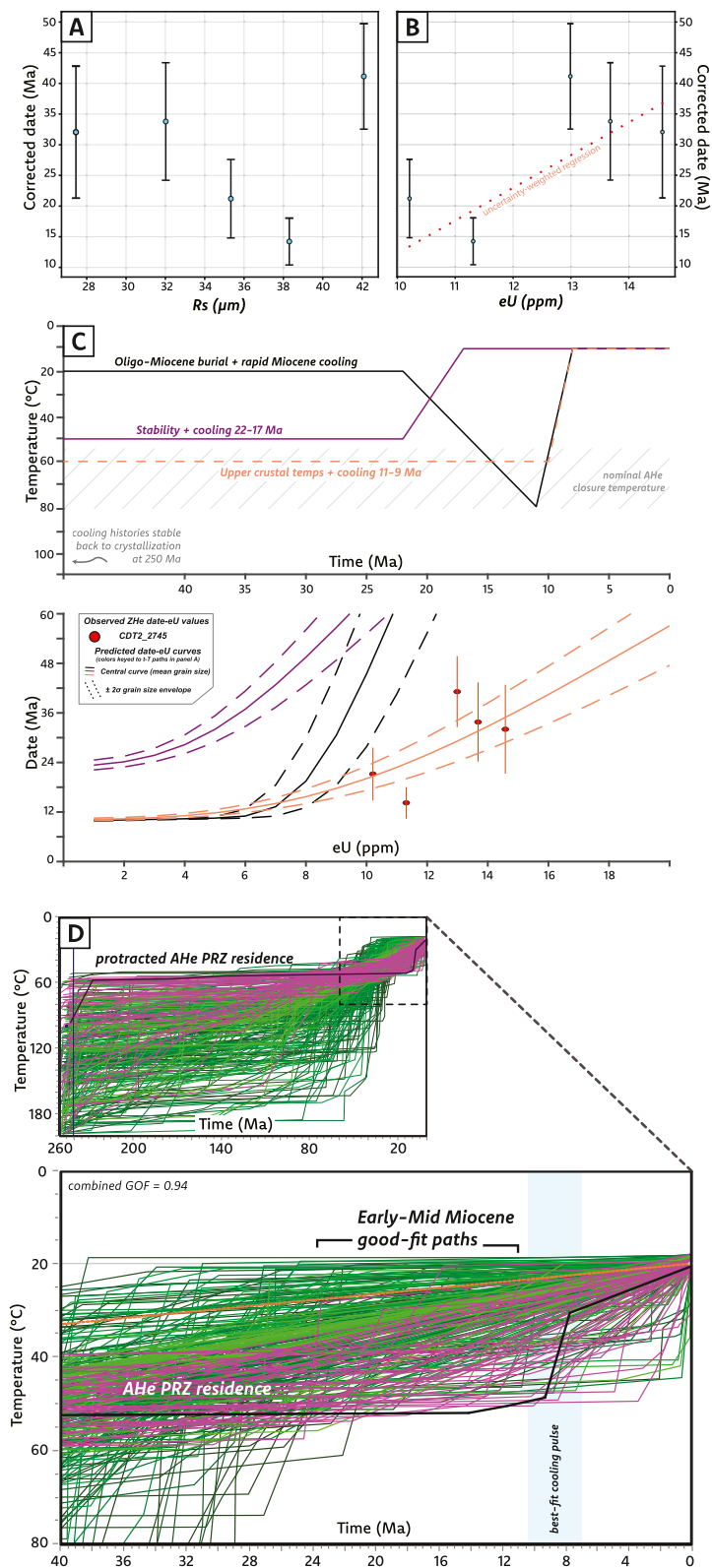


Figure 7.

best reconciles AHe dates from Cordillera del Tigre basement and upper Manantiales basin strata. This sequence of deformation is compatible with the Manantiales basin record, which records a ca. 18–16 Ma shift from transverse to internal drainage, consistent with structural damming by the Cordillera del Tigre (Ronemus et al., 2024).

## 4. Discussion

### 4.1. Regional Tectonics Surrounding the Frontal Cordillera

New bedrock thermochronology data show Early to Middle Miocene cooling of the La Ramada massif. Two periods of cooling are recorded in the hanging walls of the Santa Cruz and Espinacito faults at ca. 20 Ma and ca. 12 Ma respectively, supporting rock uplift driven erosion at this time (Figure 6b). These cooling signatures are consistent with an increase in sedimentation rate and a drainage reorganization in the Manantiales basin beginning ca. 18 Ma, likely related to tectonic loading from the shortening Principal Cordillera and Frontal Cordillera and possibly propagation of the thrust front into the Cordillera del Tigre (Mackaman-Lofland et al., 2020; Ronemus et al., 2024) (Figure 2). Additionally, growth geometries along the western margin of the Manantiales basin pin the timing of fault movement between 15 and 11 Ma (Ronemus et al., 2024). AHe dates from sample ESP2928 and the associated modeled cooling are interpreted to capture the latest stages of erosion associated with the Espinacito hanging wall at ca. 10.5 Ma (Figures 4 and 6b).

A comparison of our cooling constraints with existing thermochronology data from the eastward adjacent Precordillera demonstrates that the latter stage of deformation in the Frontal Cordillera was out-of-sequence (Figure 8). For example, the 13–9 Ma cooling documented in the hanging wall of the Espinacito fault and growth structures in the western Manantiales basin are coeval with ca. 18–2 Ma deformation in the Precordillera (Figure 8; Fosdick et al., 2015; Levina et al., 2014; Suriano et al., 2017). Mackaman-Lofland et al. (2020, 2024) suggest a kinematic linkage between the Frontal Cordillera (including the Cordillera del Tigre) and the Precordillera, with shortening sustained along a regional, broadly west-dipping décollement at depths between 10 and 20 km. Considering this geometry, the Frontal Cordillera at the latitude of Cerro Mercedario is perhaps best thought of as a basement culmination or antiformal stack like those observed in the Sevier fold-thrust belt in the western interior USA (e.g., Wasatch culmination; Yonkee, 1992; DeCelles & Coogan, 2006; Mazzitelli, 2020).

In terms of thrust belt kinematics, thermochronology evidence for exhumation at ca. 15–10 Ma is interpreted as a pulse of contraction in the Frontal Cordillera during growth of a trailing basement culmination that was feeding slip into the eastward adjacent Precordillera (Figure 8b). The onset of Cordillera del Tigre uplift and transfer of the Manantiales basin to a wedge-top position, followed by possible later out-of-sequence uplift (Figure 7), represents the eastward extent of this culmination (Figure 8c). This type of thrust belt behavior is typical of orogenic wedges that are subcritically tapered, or do not have a taper sufficient to cause forward (or in-sequence) propagation of deformation (e.g., Boyer, 1995). Widespread evidence for Middle Miocene deformation in the Principal Cordillera (e.g., Carrapa et al., 2022; Giambiagi et al., 2022) is generally consistent with internal deformation of a subcritical Andean wedge. Cristallini and Ramos (2000) discovered structural evidence for out-of-sequence thrusting in the thin-skinned La Ramada thrust belt to the west of the La Ramada massif at ca. 9 Ma, suggesting that the latter acted as a “sticking point” or buttress for deformation to the west. These interacting styles of deformation and the broader deformation chronology discussed above are partly controlled by pre-Andean structural architecture and reactivation of pre-existing normal faults related to Triassic rifting (Alvarez & Ramos, 1999). It is possible to examine the apparent kinematic sequence and structural styles at this latitude in the context of the “double-decker” model proposed by Parker and Pearson (2021) for the northern US cordilleran thrust belt. Existing restored cross sections through the La Ramada massif reveal an eastward tapering wedge of northern Neuquén basin sedimentary rocks atop the Choiyoi Group and underlying mechanical basement (Figure 8a; e.g., Cristallini & Ramos, 2000). The better constrained kinematic sequence, supported by data

**Figure 7.** AHe results from the Cordillera del Tigre segment of the Frontal Cordillera, plotted against (a) grain size (equivalent spherical radius,  $R_s$ ) and (b) effective uranium concentration (eU). (c) Forward modeling results exploring the predicted date-eU correlation from plausible time-temperature paths. All three paths begin at the Choiyoi Group crystallization age of ca. 250 Ma. Central curve represents prediction for mean grain size (35.0  $\mu\text{m}$ ), and dashed envelopes encompass  $\pm 2\sigma$  grain size. (d) HeFTy inverse modeling result from the Cordillera del Tigre. Models start with an initial T-window between 0°C and 200°C between 240 and 260 Ma representing Choiyoi Group crystallization age. Green and pink lines represent the acceptable-fit and good-fit paths, respectively. Black line represents best fit path. GOF —“goodness of fit” between model dates and measured dates.

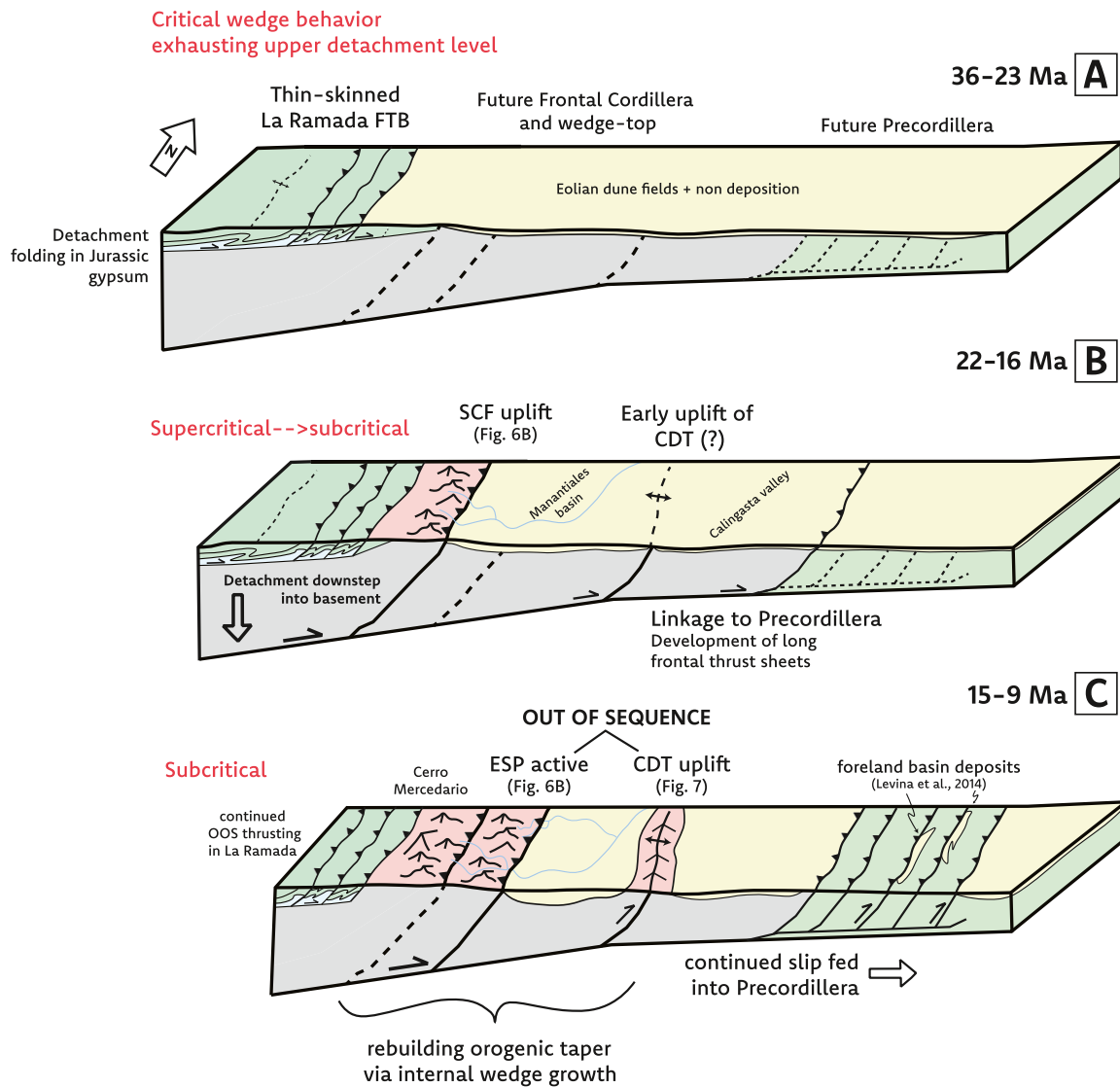


**Figure 8.** Schematic cross sections showing the preferred kinematic model for the La Ramada and Cordillera del Tigre portions of the Frontal Cordillera, relative to the eastward adjacent Precordillera. (a) Folding and thrusting in the Principal Cordillera with a detachment in weak Jurassic gypsum (e.g., Cristallini & Ramos, 2000). Mesozoic stratigraphy shown as light blue and green. To the north of the thin-skinned La Ramada thrust belt, the western Frontal Cordillera was undergoing uplift and exhumation during Late Eocene—Early Oligocene time (e.g., Fosdick et al., 2024; Lossada et al., 2017). (b) After exhausting the eastward tapering Mesozoic deposits, the basal detachment downsteps into basement (gray) and activates a linked west-dipping master detachment proposed by Mackaman-Lofland et al., 2020. Uplift and exhumation timing for the Santa Cruz hanging wall (SCF) is consistent with new thermochronology data (Figure 6B). Earliest thrusting in the western Precordillera (Jordan et al., 2001; Levina et al., 2014). Exposure of the Choiyoi Group overlying the basement is shown schematically with rose color mountainous topography. (c) New thermochronology data resolves out-of-sequence thrusting for the Espinacito fault and Cordillera del Tigre (ESP and CDT, respectively). Both structures were active during the peak of shortening in the Precordillera. A kinematic linkage between the Frontal Cordillera and Precordillera is compatible with new thermochronology data, with out-of-sequence cooling pulses representing internal growth of an eastward propagating orogenic wedge. Yellow schematically represents Cenozoic basin fill.

presented here, involves early exploitation of weak Jurassic salt units (e.g., Cristallini et al., 1995) followed by activation (or reactivation) of deeper west-dipping faults that ultimately were responsible for uplift and exhumation of the La Ramada massif (e.g., Santa Cruz fault). The main decollement and associated orogenic wedge stepping down into deeper structural levels as the thrust belt exhausted the weak overlying horizons, followed by eastward propagation and the linkage of Frontal Cordillera structures with those in the adjacent Precordillera is compatible with the expected behavior of supercritical to subcritical cycles of thrust belts with limited stratigraphy atop basement (Figures 8b and 8c; e.g., Coogan, 1992). Although a somewhat isolated example, the study of

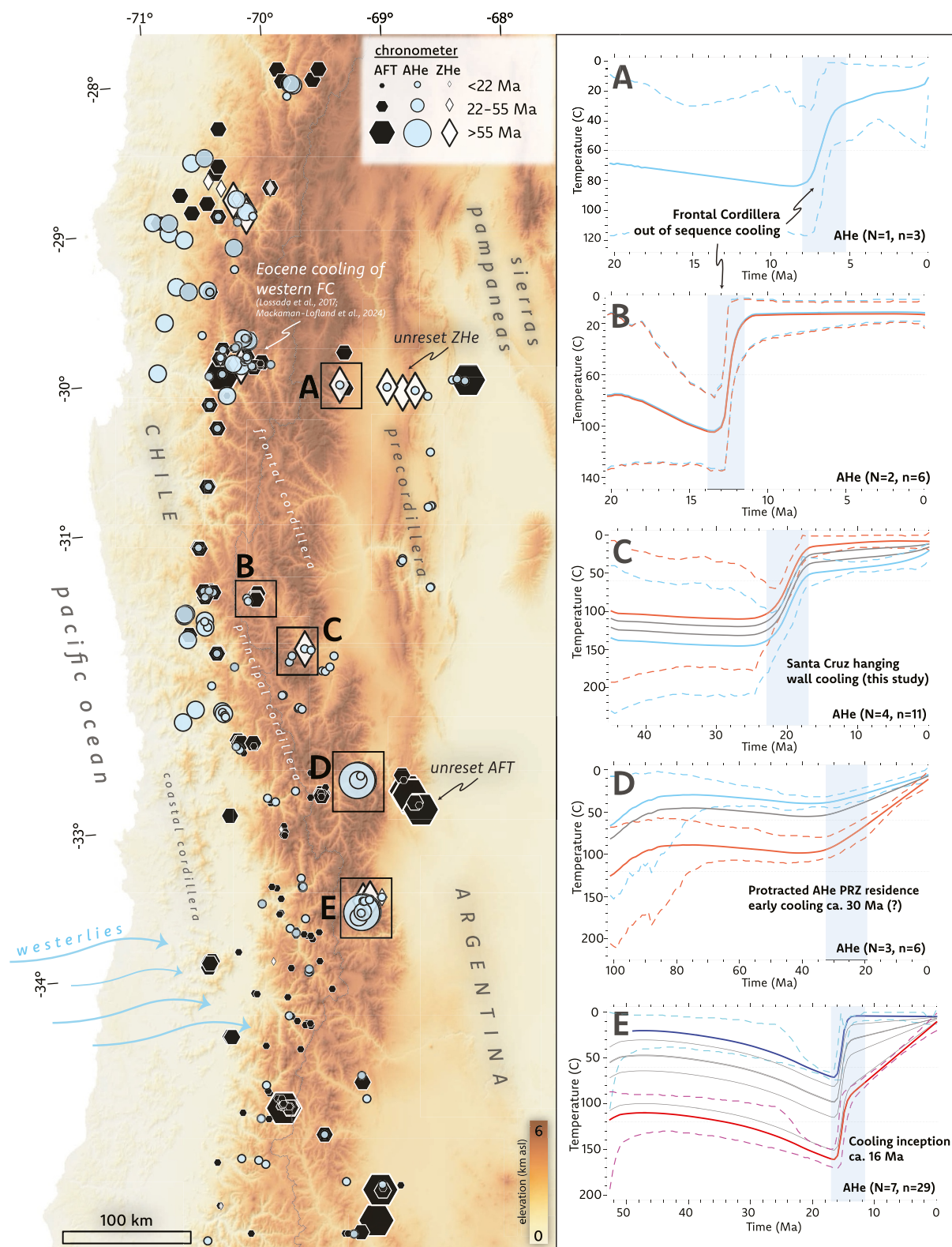


Figure 9.

La Ramada massif and other regions to the south with limited shortening and complex, relatively thin sedimentary packages atop basement will benefit from considerations using this deformation framework.

#### 4.2. Exhumation Along Strike of the Frontal Cordillera

Several thermochronology data sets along strike of the Frontal Cordillera have high single-grain variability and/or poorly behaved fission-tracks, precluding straight-forward interpretations of cooling histories. As demonstrated above, thermal history modeling is a helpful approach to test hypotheses and potentially extract thermal information from dispersed samples. We utilized QTQt to invert apatite (U-Th-Sm)/He data from select Frontal Cordillera transects and consider our results in the context of an updated compilation of thermochronology data from the south-central Andes (Figure 9; Data Set S2 and S4). Results include examples of the interpreted out-of-sequence cooling pulses mentioned above (Figures 9a and 9b), as well as Early to Middle Miocene cooling of the La Ramada massif and the Frontal Cordillera at more southern latitudes (Figures 9c and 9e).

The data sets along strike in Figure 9 have fueled a debate regarding the overall vergence direction of the south-central Andean thrust belt (e.g., Lossada et al., 2023; Riesner et al., 2019). Although Eocene cooling has been documented to the north of Cerro Mercedario (Fosdick et al., 2024; Lossada et al., 2017; Mackaman-Lofland et al., 2024), existing data south of Mercedario point toward a Miocene onset of rapid cooling for the Frontal Cordillera. This appears to be consistent along strike (Figure 9; Lossada et al., 2018) with possible complications related to varying amounts of foredeep burial and paleotopographic highs that existed before Andean deformation (e.g., Hoke et al., 2014; Figure 9d). There is primarily uncertainty in the southern region surrounding whether the onset of cooling was during the Early, Middle, or Late Miocene. The ca. 22–20 Ma “early” cooling suggested by Riesner et al. (2019) has been used as evidence for an overall west-vergent Andean system with shortening sustained along an east-dipping crustal scale footwall ramp. This contrasts with a later (ca. 15 Ma) onset of rapid uplift and exhumation following a generally in sequence pattern of deformation with the westward adjacent Principal Cordillera (e.g., Lossada et al., 2023). QTQt thermal history inversion results combining AHe data from Riesner et al. (2019) and Lossada et al. (2023) are consistent with the timing of cooling determined by the latter, beginning at ca. 16 Ma (Figure 9e). Early- to Middle Miocene uplift of the Frontal Cordillera along strike is supported by partially reset AHe dates implying that foreland basin deposits were not sufficiently thick to reset the chronometer, as well as abundant evidence that Miocene basin deposits were accumulating in a discontinuous foreland (probably wedgetop) position (e.g., Lossada et al., 2023; Ronemus et al., 2024). Paired with recent findings from the foreland basin record, thermochronology data from Cerro Mercedario and the Cordillera del Tigre are consistent with east-vergent mountain building punctuated by out-of-sequence deformation (Figure 8; Ronemus et al., 2024). Similar kinematics may explain the apparent chronology of deformation to the south without the need for major changes in the geometry of the main crustal-scale faults (i.e., Giambiagi et al., 2012).

Recent thermochronology studies at 30°S have documented convincing evidence of Late Eocene exhumation of the Frontal Cordillera (Fosdick et al., 2024; Mackaman-Lofland et al., 2024), whereas our data set and those to the south of Cerro Mercedario at 32°S are confined mostly to the Miocene (Figure 9). The northern region also coincides with thicker foreland basin deposits in the Bermejo Basin that taper to the south (Jordan et al., 2001), potentially suggesting a larger orogenic load at this latitude. This implies that uplift and exhumation may have begun earlier in the northern Frontal Cordillera. The absence of Eocene-Oligocene cooling and the thinning of foreland basin deposits to the south (Jordan et al., 2001) could reflect later activation of lower detachment levels and tectonic loading in the La Ramada region during the Miocene (Figure 9).

We emphasize that thermochronology data in the south-central Andes should be interpreted with caution due to the prevalence of out-of-sequence thrusting. Such thrust belt behavior complicates a straight-forward interpretation of thermochronology data with regards to deformation vergence. Given its large areal extent and

**Figure 9.** Variable cooling histories from select transects along strike of the Frontal Cordillera determined by inverse thermal history modeling of apatite (U-Th-Sm)/He data. Transects placed in the context of existing thermochronology data from the south-central Andes (symbols represent different chronometers, size of symbols increases proportional to age/date). Letters for each time-temperature path are keyed to the map and only portions of the time-temperature history constrained by the input data are displayed (note varying *x*-axis). Light blue bar highlights approximate onset of Cenozoic cooling. References for each inversion: (a) Fosdick et al. (2015), (b) Maydagán et al. (2020), (c) this study, (d) Hoke et al. (2015), (e) Riesner et al. (2019), and Lossada et al. (2023). Thermochronology data compilation available as Data Set S4.

significance in the context of ongoing tectonic arguments in the south-central Andes, continued generation of low-temperature thermochronology data from the Frontal Cordillera is essential.

### 4.3. Regional Tectono-Climatic Implications

The Frontal Cordillera represents a deeply exhumed tectonic province in the south-central Andes relative to the westward adjacent Principal Cordillera, with almost complete erosion of the Mesozoic-present stratigraphy (e.g., Cristallini & Ramos, 2000; Ramos et al., 1996). The fact that the ZHe dates in this and comparable studies (Riesner et al., 2019) are partially reset underscores the simple but important point that the magnitude of erosion in the hinterland of the highest Andes is low (i.e., not high enough to expose fully reset chronometers). The lack of young (<5 Ma) AHe dates in the La Ramada massif contrasts with existing results from low-temperature thermochronometers on both sides of the Andean drainage divide south of 33°S (Figure 9), many of which are younger than what is recorded by our transect (e.g., Farias et al., 2008; Stalder et al., 2020). Val et al. (2018) highlighted that focused seismicity and rock uplift, rather than changes in precipitation, are responsible for the latitudinal changes in erosion rate. Our new data reinforce the fact that apparently limited erosion and topography formation has occurred since the Miocene (i.e., during Plio-Pleistocene glaciations) in the La Ramada massif and other regions of the High Andes north of Cerro Aconcagua (e.g., Bissig et al., 2002, 2003; Hoke et al., 2014).

## 5. Conclusions

- New field and low temperature thermochronology data from the La Ramada massif are consistent with Early to Middle Miocene exhumation along the Santa Cruz and Espinacito reverse faults. Thermal history models suggest thrust-related cooling at ca. 20 and 12 Ma. Although these cooling signals appear to be in-sequence from west to east, cooling along the Espinacito fault is out-of-sequence relative to the Cordillera del Tigre and Precordillera which were actively uplifting as early as 18 Ma (Fosdick et al., 2015; Jordan et al., 2001; Ronemus et al., 2024). The timing of out-of-sequence deformation along the Espinacito fault determined in this study is compatible with recently constrained growth structures in the Manantiales wedge-top basin.
- AHe dates from the Cordillera del Tigre portion of the Frontal Cordillera suggest that overlying foredeep deposits were not thick enough to reset the chronometer (<2.5 km). Partially reset dates from the base of the range in tandem with reset AHe dates from upper Manantiales basin strata are consistent with early uplift of the Cordillera del Tigre and transfer of the basin to a wedge-top position during the early to mid-Miocene. An out-of-sequence pulse of uplift and exhumation at ca. 11–9 Ma is suggested by AHe forward models from the CDT.
- Relief in this segment of the Frontal Cordillera formed during the Miocene (e.g., Hoke et al., 2015), suggesting that shortening was a primary control on surface uplift. Relatively high shortening has occurred in the Precordillera to the east coeval with continued deformation and erosion in the High Andes along the Argentina-Chile border.
- Comparisons with existing thermochronologic data sets to the south reveals consistency in Early to Middle Miocene rapid cooling along strike of the Frontal Cordillera. Although this timing has been interpreted to suggest both a west- and east-vergent orogenic system, we emphasize that regional trends in bedrock thermochronology and the adjacent basin record are consistent with forward propagation and internal deformation of an overall east-vergent fold-thrust belt.

## Data Availability Statement

Detailed grain descriptions and dimension measurements for apatite (U-Th-Sm)/He and zircon (U-Th)/He are available in Data Set S1 at Zenodo via <https://doi.org/10.5281/zenodo.11152585> with no access restrictions (Howlett et al., 2024). All QTQt thermal history modeling input and output files are available in Data Set S2 at Zenodo via <https://doi.org/10.5281/zenodo.11152585> with no access restrictions (Howlett et al., 2024). QTQt model input parameters and decisions made are available in Data Set S3 at Zenodo via <https://doi.org/10.5281/zenodo.11152585> with no access restrictions (Howlett et al., 2024). Compilation of

existing and new low-temperature thermochronology data in the south-central Andes is available in Data Set S4 at Zenodo via <https://doi.org/10.5281/zenodo.11152585> with no access restrictions (Howlett et al., 2024). A supplementary video documenting the sampling transect is available at <https://youtu.be/luIKT0mtfYO4> (Howlett, 2024).

## Acknowledgments

Funding provided by U.S. National Science Foundation Grant EAR2020935. We thank Chelsea Mackaman-Lofland, Laura Giambiagi, Julieta Suriano, and colleagues at Instituto Argentino de Nivología, Glaciología y Ciencias Ambientales, Mendoza, AR for discussion and logistical assistance. Uttam Chowdury is appreciated for helium assistance. Editor Taylor Schildgen, Alyssa Abbey, two anonymous reviewers, and the associate editor provided critical comments that helped us to improve the manuscript.

## References

- Abbey, A. L., Wildman, M., Stevens Goddard, A. L., & Murray, K. E. (2023). Thermal history modeling techniques and interpretation strategies: Applications using QTQt. *Geosphere*, 19(2), 493–530. <https://doi.org/10.1130/GES02528.1>
- Alarcón, P., & Pinto, L. (2015). Neogene erosion of the Andean Cordillera in the flat-slab segment as indicated by petrography and whole-rock geochemistry from the Manantiales Foreland Basin (32°–32°30'S). *Tectonophysics*, 639, 1–22. <https://doi.org/10.1016/j.tecto.2014.11.001>
- Allmendinger, R. W., Figueroa, D., Snyder, D., Beer, J., Mpodozis, C., & Isacks, B. L. (1990). Foreland shortening and crustal balancing in the Andes at 30°S latitude. *Tectonics*, 9(4), 789–809. <https://doi.org/10.1029/TC009i004p00789>
- Alvarez, P. P., Benoit, S. V., & Ottone, E. G. (1995). Las Formaciones Rancho de Lata, Los Patillos y otras unidades Mesozoicas de la Cordillera Principal de San Juan. *Revista de la Asociación Geológica Argentina*, 49(1–2), 133–152.
- Alvarez, P. P., & Ramos, V. A. (1999). The Mercedario rift system in the principal Cordillera of Argentina and Chile (32° SL). *Journal of South American Earth Sciences*, 12(1), 17–31. [https://doi.org/10.1016/S0895-9811\(99\)00004-8](https://doi.org/10.1016/S0895-9811(99)00004-8)
- Anderson, R. B., Long, S. P., Horton, B. K., Thomson, S. N., Calle, A. Z., & Stockli, D. F. (2018). Orogenic wedge evolution of the Central Andes, Bolivia (21°S): Implications for cordilleran cyclicity. *Tectonics*, 37(10), 3577–3609. <https://doi.org/10.1029/2018TC005132>
- Ault, A. K., Guenther, W. R., Moser, A. C., Miller, G. H., & Refsnider, K. A. (2018). Zircon grain selection reveals (de)coupled metamictization, radiation damage, and He diffusivity. *Chemical Geology*, 490, 1–12. <https://doi.org/10.1016/j.chemgeo.2018.04.023>
- Bissig, T., Clark, A. H., Lee, J. K. W., & Hodgson, C. J. (2002). Miocene landscape evolution and geomorphologic controls on epithermal processes in the El Indio-Pascua Au-Ag-Cu Belt, Chile and Argentina. *Economic Geology*, 97(5), 971–996. <https://doi.org/10.2113/gsecongeo.97.5.971>
- Bissig, T., Clark, A. H., Lee, J. K. W., & Von Quadt, A. (2003). Petrogenetic and metallogenetic responses to Miocene slab flattening: New constraints from the El Indio-Pascua Au–Ag–Cu belt, Chile/Argentina. *Mineralium Deposita*, 38(7), 844–862. <https://doi.org/10.1007/s00126-003-0375-y>
- Boyer, S. E. (1995). Sedimentary basin taper as a factor controlling the geometry and advance of thrust belts. *American Journal of Science*, 295(10), 1220–1254. <https://doi.org/10.2475/ajs.295.10.1220>
- Braun, J., Beek, P. V. D., & Batt, G. (2006). *Quantitative thermochronology: Numerical methods for the interpretation of thermochronological data* (1st ed.). Cambridge University Press. <https://doi.org/10.1017/CBO9780511616433>
- Buelow, E. K., Suriano, J., Mahoney, J. B., Kimbrough, D. L., Mescua, J. F., Giambiagi, L. B., & Hoke, G. D. (2018). Sedimentologic and stratigraphic evolution of the Cacheuta basin: Constraints on the development of the Miocene retroarc foreland basin, south-central Andes. *Lithosphere*, 10(3), 366–391. <https://doi.org/10.1130/L709.1>
- Cahill, T., & Isacks, B. L. (1992). Seismicity and shape of the subducted Nazca Plate. *Journal of Geophysical Research*, 97(B12), 17503–17529. <https://doi.org/10.1029/92JB00493>
- Carrapa, B., DeCelles, P. G., Ducea, M. N., Jepson, G., Osakwe, A., Balgord, E., et al. (2022). Estimates of paleo-crustal thickness at Cerro Aconcagua (Southern Central Andes) from detrital proxy-records: Implications for models of continental arc evolution. *Earth and Planetary Science Letters*, 585, 117526. <https://doi.org/10.1016/j.epsl.2022.117526>
- Coogan, J. C. (1992). Chapter 2: Structural evolution of piggyback basins in the Wyoming-Idaho-Utah thrust belt. In *Geological society of America memoirs* (Vol. 179, pp. 55–82). Geological Society of America. <https://doi.org/10.1130/MEM179-p55>
- Cooperdock, E. H. G., Ketcham, R. A., & Stockli, D. F. (2019). Resolving the effects of 2-D versus 3-D grain measurements on apatite (U–Th)/He age data and reproducibility. *Geochronology*, 1(1), 17–41. <https://doi.org/10.5194/gchron-1-17-2019>
- Cristallini, E., Mosquera, A., & Ramos, V. A. (1995). Estructura de la Alta cordillera de San Juan. *Asociación Geológica Argentina Buenos Aires, Revista*, 49(1/2), 165–183.
- Cristallini, E. O., & Ramos, V. A. (2000). Thick-skinned and thin-skinned thrusting in the La Ramada fold and thrust belt: Crustal evolution of the high Andes of San Juan, Argentina (32°SL). *Tectonophysics*, 317(3–4), 205–235. [https://doi.org/10.1016/S0040-1951\(99\)00276-0](https://doi.org/10.1016/S0040-1951(99)00276-0)
- Dahlquist, J. A., Morales Cámara, M. M., Santos Da Cruz, G., Basei, M. A. S., Moreno, J. A., Rocher, S., et al. (2024). Generation and evolution of the Choiyoi granitic magmatism based on U–Pb zircon studies, Cordón del Portillo, Frontal Cordillera (Argentina). *Journal of South American Earth Sciences*, 147, 105134. <https://doi.org/10.1016/j.jsames.2024.105134>
- Dávila, F. M., Astini, R. A., Jordan, T. E., Gehrels, G., & Ezpeleta, M. (2007). Miocene forebulge development previous to broken foreland partitioning in the southern Central Andes, west-central Argentina. *Tectonics*, 26(5), 2007TC002118. <https://doi.org/10.1029/2007TC002118>
- Dávila, F. M., Lithgow-Bertelloni, C., & Giménez, M. (2010). Tectonic and dynamic controls on the topography and subsidence of the Argentine Pampas: The role of the flat slab. *Earth and Planetary Science Letters*, 295(1–2), 187–194. <https://doi.org/10.1016/j.epsl.2010.03.039>
- DeCelles, P. G., & Coogan, J. C. (2006). Regional structure and kinematic history of the Sevier fold-and-thrust belt, central Utah. *Geological Society of America Bulletin*, 118(7–8), 841–864. <https://doi.org/10.1130/B25759.1>
- DeCelles, P. G., & Giles, K. A. (1996). Foreland basin systems. *Basin Research*, 8(2), 105–123. <https://doi.org/10.1046/j.1365-2117.1996.01491.x>
- England, P., & Molnar, P. (1990). Surface uplift, uplift of rocks, and exhumation of rocks. *Geology*, 18(12), 1173. [https://doi.org/10.1130/0091-7613\(1990\)018<1173:SUUORA>2.3.CO;2](https://doi.org/10.1130/0091-7613(1990)018<1173:SUUORA>2.3.CO;2)
- Fariás, M., Charrier, R., Carretier, S., Martinod, J., Fock, A., Campbell, D., et al. (2008). Late Miocene high and rapid surface uplift and its erosional response in the Andes of central Chile (33°–35°S). *Tectonics*, 27(1), 2006TC002046. <https://doi.org/10.1029/2006TC002046>
- Farley, K. A., & Stockli, D. F. (2002). (U–Th)/He dating of phosphates: Apatite, monazite, and xenotime. *Reviews in Mineralogy and Geochemistry*, 48(1), 559–577. <https://doi.org/10.2138/rmg.2002.48.15>
- Farley, K. A., Wolf, R. A., & Silver, L. T. (1996). The effects of long alpha-stopping distances on (U–Th)/He ages. *Geochimica et Cosmochimica Acta*, 60(21), 4223–4229. [https://doi.org/10.1016/S0016-7037\(96\)00193-7](https://doi.org/10.1016/S0016-7037(96)00193-7)
- Fennell, L. M., Martos, F. E., Peluffo, N. A., Acevedo, E., Fernández Paz, L., Morel, L., et al. (2023). The classical Cuevas River section revisited: An update to the style and timing of deformation of the Aconcagua region based on new geological, structural and geochronological data (32° 50'S). *Frontiers in Earth Science*, 11, 1219351. <https://doi.org/10.3389/feart.2023.1219351>

- Fitzgerald, P. G., Baldwin, S. L., Webb, L. E., & O'Sullivan, P. B. (2006). Interpretation of (U–Th)/He single grain ages from slowly cooled crustal terranes: A case study from the Transantarctic Mountains of southern Victoria Land. *Chemical Geology*, 225(1–2), 91–120. <https://doi.org/10.1016/j.chemgeo.2005.09.001>
- Fitzgerald, P. G., Sorkhabi, R. B., Redfield, T. F., & Stump, E. (1995). Uplift and denudation of the central Alaska Range: A case study in the use of apatite fission track thermochronology to determine absolute uplift parameters. *Journal of Geophysical Research*, 100(B10), 20175–20191. <https://doi.org/10.1029/95JB02150>
- Flowers, R. M., Ketcham, R. A., Shuster, D. L., & Farley, K. A. (2009). Apatite (U–Th)/He thermochronometry using a radiation damage accumulation and annealing model. *Geochimica et Cosmochimica Acta*, 73(8), 2347–2365. <https://doi.org/10.1016/j.gca.2009.01.015>
- Fosdick, J. C., Carrapa, B., & Ortíz, G. (2015). Faulting and erosion in the Argentine Precordillera during changes in subduction regime: Reconciling bedrock cooling and detrital records. *Earth and Planetary Science Letters*, 432, 73–83. <https://doi.org/10.1016/j.epsl.2015.09.041>
- Fosdick, J. C., Stevens Goddard, A. L., Mackaman-Lofland, C., Lossada, A. C., Rodríguez, M. P., & Carrapa, B. (2024). Eocene exhumation of the High Andes at ~30°S differentiated by detrital multimethod U–Pb–He thermochronology. *Geology*, 52(9), 678–682. <https://doi.org/10.1130/G52272.1>
- Gallagher, K. (2012). Transdimensional inverse thermal history modeling for quantitative thermochronology. *Journal of Geophysical Research*, 117(B2), 2011JB008825. <https://doi.org/10.1029/2011JB008825>
- Gans, C. R., Beck, S. L., Zandt, G., Gilbert, H., Alvarado, P., Anderson, M., & Linkimer, L. (2011). Continental and oceanic crustal structure of the Pampean flat slab region, western Argentina, using receiver function analysis: New high-resolution results: Seismic imaging of the Pampean flat slab. *Geophysical Journal International*, 186(1), 45–58. <https://doi.org/10.1111/j.1365-246X.2011.05203.x>
- Giambiagi, L., Mescua, J., Bechis, F., Tassara, A., & Hoke, G. (2012). Thrust belts of the southern Central Andes: Along-strike variations in shortening, topography, crustal geometry, and denudation. *Geological Society of America Bulletin*, 124(7–8), 1339–1351. <https://doi.org/10.1130/B30609.1>
- Giambiagi, L., Tassara, A., Echaurren, A., Julve, J., Quiroga, R., Barrionuevo, M., et al. (2022). Crustal anatomy and evolution of a subduction-related orogenic system: Insights from the Southern Central Andes (22–35°S). *Earth-Science Reviews*, 232, 104138. <https://doi.org/10.1016/j.earscirev.2022.104138>
- Guenther, W. R., Reiners, P. W., Ketcham, R. A., Nasdala, L., & Giester, G. (2013). Helium diffusion in natural zircon: Radiation damage, anisotropy, and the interpretation of zircon (U–Th)/He thermochronology. *American Journal of Science*, 313(3), 145–198. <https://doi.org/10.2475/03.2013.01>
- Härtel, B., Jonckheere, R., Krause, J., & Ratschbacher, L. (2022). Spurious age-eU associations in thermochronological data. *Earth and Planetary Science Letters*, 599, 117870. <https://doi.org/10.1016/j.epsl.2022.117870>
- Hayes, G. P., Moore, G. L., Portner, D. E., Hearne, M., Flamme, H., Furtney, M., & Smoczyk, G. M. (2018). Slab2, a comprehensive subduction zone geometry model. *Science*, 362(6410), 58–61. <https://doi.org/10.1126/science.aat4723>
- He, J., Thomson, S. N., Reiners, P. W., Hemming, S. R., & Licht, K. J. (2021). Rapid erosion of the central Transantarctic Mountains at the Eocene-Oligocene transition: Evidence from skewed (U–Th)/He date distributions near Beardmore Glacier. *Earth and Planetary Science Letters*, 567, 117009. <https://doi.org/10.1016/j.epsl.2021.117009>
- Hoke, G. D., Giambiagi, L. B., Garzione, C. N., Mahoney, J. B., & Strecker, M. R. (2014). Neogene paleoelevation of intermontane basins in a narrow, compressional mountain range, southern Central Andes of Argentina. *Earth and Planetary Science Letters*, 406, 153–164. <https://doi.org/10.1016/j.epsl.2014.08.032>
- Hoke, G. D., Graber, N. R., Mescua, J. F., Giambiagi, L. B., Fitzgerald, P. G., & Metcalf, J. R. (2015). Near pure surface uplift of the Argentine Frontal Cordillera: Insights from (U–Th)/He thermochronometry and geomorphic analysis. *Geological Society, London, Special Publications*, 399(1), 383–399. <https://doi.org/10.1144/SP399.4>
- Horton, B. K. (2018). Tectonic regimes of the central and southern Andes: Responses to variations in plate coupling during subduction. *Tectonics*, 37(2), 402–429. <https://doi.org/10.1002/2017TC004624>
- Howlett, C. J. (2024). Geologists climb a 6700m peak in the Andes | Cerro Mercedario. [Supporting Video]. Retrieved from <https://youtu.be/uiKT0mtfYO4>
- Howlett, C. J., Ronemus, C. B., Carrapa, B., & DeCelles, P. G. (2024). Miocene construction of the High Andes recorded by exhumation of the Frontal Cordillera, La Ramada Massif of western Argentina (32°S) (supporting information) (version 1) [Dataset]. *Zenodo*. <https://doi.org/10.5281/zenodo.11152585>
- Huntington, K. W., Ehlers, T. A., Hodges, K. V., & Whipp, D. M. (2007). Topography, exhumation pathway, age uncertainties, and the interpretation of thermochronometer data. *Tectonics*, 26(4), 2007TC002108. <https://doi.org/10.1029/2007TC002108>
- Introcaso, A., Pacino, M. C., & Fraga, H. (1992). Gravity, isostasy and Andean crustal shortening between latitudes 30 and 35°S. *Tectonophysics*, 205(1–3), 31–48. [https://doi.org/10.1016/0040-1951\(92\)90416-4](https://doi.org/10.1016/0040-1951(92)90416-4)
- Jordan, T. E., Schlunegger, F., & Cardozo, N. (2001). Unsteady and spatially variable evolution of the Neogene Andean Bermejo foreland basin, Argentina. *Journal of South American Earth Sciences*, 14(7), 775–798. [https://doi.org/10.1016/s0895-9811\(01\)00072-4](https://doi.org/10.1016/s0895-9811(01)00072-4)
- Jordan, T. E., Tamm, V., Figueroa, G., Flemings, P. B., Richards, D., Tabbutt, K., & Cheatham, T. (1996). Development of the Miocene Manantiales foreland basin, Principal Cordillera, San Juan, Argentina. *Andean Geology*, 23(1), 43–79.
- Ketcham, R. A. (2024). Thermal history inversion from thermochronometric data and complementary information: New methods and recommended practices. *Chemical Geology*, 653, 122042. <https://doi.org/10.1016/j.chemgeo.2024.122042>
- Lencinas, A. (1982). Características estructurales del extremo sur Hidrocarburos, Actas II 325–336. de la cordillera Sanjuanina, Argentina. V° Congreso Lati, Cristallini, E.O., Ramos, V.A., 1995. *Structural cross-section noamericano de Geología, Actas, I*, 489–498.
- Levina, M., Horton, B. K., Fuentes, F., & Stockli, D. F. (2014). Cenozoic sedimentation and exhumation of the foreland basin system preserved in the Precordillera thrust belt (31–32°S), southern central Andes, Argentina: Precordillera thrust belt evolution. *Tectonics*, 33(9), 1659–1680. <https://doi.org/10.1002/2013TC003424>
- Lossada, A. C., Giambiagi, L., Hoke, G., Mescua, J., Suriano, J., & Mazzitelli, M. (2018). Cenozoic uplift and exhumation of the frontal cordillera between 30° and 35°S and the influence of the subduction dynamics in the flat slab subduction context, south Central Andes. In A. Folguera, E. Contreras-Reyes, N. Heredia, A. Encinas, S. B. Iannelli, V. Oliveros, et al. (Eds.), *The evolution of the Chilean-Argentinean Andes* (pp. 387–409). Springer International Publishing. [https://doi.org/10.1007/978-3-319-67774-3\\_16](https://doi.org/10.1007/978-3-319-67774-3_16)
- Lossada, A. C., Giambiagi, L., Hoke, G. D., Fitzgerald, P. G., Creixell, C., Murillo, I., et al. (2017). Thermochronologic evidence for late Eocene Andean mountain building at 30°S: Eocene Andean mountain building at 30°S. *Tectonics*, 36(11), 2693–2713. <https://doi.org/10.1002/2017TC004674>
- Lossada, A. C., Giambiagi, L. B., Mescua, J. F., Suriano, J., Ramos, M. E., Barrionuevo, M., & Arzadún, G. (2023). Exhumation timing of the Cordón del Portillo, Frontal Cordillera, supports the east-vergent model for the growth of the southern central Andes. *Journal of South American Earth Sciences*, 121, 104150. <https://doi.org/10.1016/j.jsames.2022.104150>

- Lossada, A. C., Hoke, G. D., Giambiagi, L. B., Fitzgerald, P. G., Mescua, J. F., Suriano, J., & Aguilar, A. (2020a). Detrital thermochronology reveals major middle Miocene exhumation of the eastern flank of the Andes that predates the Pampean flat slab (33°–33.5°S). *Tectonics*, 39(4), e2019TC005764. <https://doi.org/10.1029/2019TC005764>
- Lossada, A. C., Suriano, J., Giambiagi, L., Fitzgerald, P. G., Hoke, G., Mescua, J., et al. (2020b). Cenozoic exhumation history at the core of the Andes at 31.5°S revealed by apatite fission track thermochronology. *Journal of South American Earth Sciences*, 103, 102751. <https://doi.org/10.1016/j.jsames.2020.102751>
- Mackaman-Lofland, C., Horton, B. K., Fuentes, F., Constenius, K. N., Ketcham, R. A., Capaldi, T. N., et al. (2020). Andean mountain building and foreland basin evolution during thin- and thick-skinned Neogene deformation (32–33°S). *Tectonics*, 39(3), e2019TC005838. <https://doi.org/10.1029/2019TC005838>
- Mackaman-Lofland, C., Horton, B. K., Fuentes, F., Constenius, K. N., & Stockli, D. F. (2019). Mesozoic to Cenozoic retroarc basin evolution during changes in tectonic regime, southern Central Andes (31–33°S): Insights from zircon U-Pb geochronology. *Journal of South American Earth Sciences*, 89, 299–318. <https://doi.org/10.1016/j.jsames.2018.10.004>
- Mackaman-Lofland, C., Lossada, A. C., Fosdick, J. C., Litvak, V. D., Rodríguez, M. P., Bertoa Del Llano, M., et al. (2024). Unraveling the tectonic evolution of the Andean hinterland (Argentina and Chile, 30°S) using multi-sample thermal history models. *Earth and Planetary Science Letters*, 643, 118888. <https://doi.org/10.1016/j.epsl.2024.118888>
- Martin, P. E., Metcalf, J. R., & Flowers, R. M. (2023). Calculation of uncertainty in the (U-Th)/He system. *Geochronology*, 5(1), 91–107. <https://doi.org/10.5194/gchron-5-91-2023>
- Maydagan, L., Franchini, M., Chiaradia, M., Dilles, J., & Rey, R. (2014). The altar porphyry Cu-(Au-Mo) deposit (Argentina): A complex magmatic-hydrothermal system with evidence of recharge processes. *Economic Geology*, 109(3), 621–641. <https://doi.org/10.2113/econgeo.109.3.621>
- Maydagán, L., Zattin, M., Mpodozis, C., Selby, D., Franchini, M., & Dimieri, L. (2020). Apatite (U-Th)/He thermochronology and Re-Os ages in the altar region, Central Andes (31°30'S), main Cordillera of San Juan, Argentina: Implications of rapid exhumation in the porphyry Cu (Au) metal endowment and regional tectonics. *Mineralium Deposita*, 55(7), 1365–1384. <https://doi.org/10.1007/s00126-019-00946-9>
- Mazzitelli, M. A. (2020). *Interacción entre procesos tectónicos profundos y superficiales a lo largo de la transecta Cerro Mercedario (32°S), Andes Centrales Sur (PhD Thesis)*. Universidad Nacional de La Plata.
- McQuarrie, N. (2002). The kinematic history of the central Andean fold-thrust belt, Bolivia: Implications for building a high plateau. *Geological Society of America Bulletin*, 114(8), 950–963. [https://doi.org/10.1130/0016-7606\(2002\)114<0950:TKHOTC>2.0.CO;2](https://doi.org/10.1130/0016-7606(2002)114<0950:TKHOTC>2.0.CO;2)
- Milesi, G., Monié, P., Münch, P., Soliva, R., Taillefer, A., Bruguier, O., et al. (2020). Tracking geothermal anomalies along a crustal fault using (U-Th)/He apatite thermochronology and rare-earth element (REE) analyses: The example of the Têt fault (Pyrenees, France). *Solid Earth*, 11(5), 1747–1771. <https://doi.org/10.5194/se-11-1747-2020>
- Milesi, G., Soliva, R., Monié, P., Münch, P., Bellanger, M., Bruguier, O., et al. (2019). Mapping a geothermal anomaly using apatite (U-Th)/He thermochronology in the Têt fault damage zone, eastern Pyrenees, France. *Terra Nova*, 31(6), 569–576. <https://doi.org/10.1111/ter.12429>
- Mpodozis, C., & Kay, S. M. (1992). Late Paleozoic to Triassic evolution of the Gondwana margin: Evidence from Chilean Frontal Cordilleran batholiths (28°S to 31°S). *Geological Society of America Bulletin*, 104(8), 999–1014. [https://doi.org/10.1130/0016-7606\(1992\)104<0999:LPTTEO>2.3.CO;2](https://doi.org/10.1130/0016-7606(1992)104<0999:LPTTEO>2.3.CO;2)
- Orme, D. A., Guenther, W. R., Laskowski, A. K., & Reiners, P. W. (2016). Long-term tectonothermal history of Laramide basement from zircon-He age-eU correlations. *Earth and Planetary Science Letters*, 453, 119–130. <https://doi.org/10.1016/j.epsl.2016.07.046>
- Parker, S. D., & Pearson, D. M. (2021). Pre-thrusting stratigraphic control on the transition from a thin-skinned to thick-skinned structural style: An example from the double-decker Idaho-montana fold-thrust belt. *Tectonics*, 40(5), 1–31. <https://doi.org/10.1029/2020TC006429>
- Pérez, D. J. (1995). *Estudio geológico del Cordón del Espinacito y regiones adyacentes, provincial de San Juan (PhD Thesis)*. Universidad de Buenos Aires.
- Pinto, L., Alarcón, P., Morton, A., & Naipauer, M. (2018). Geochemistry of heavy minerals and U-Pb detrital zircon geochronology in the Manantiales Basin: Implications for Frontal Cordillera uplift and foreland basin connectivity in the Andes of central Argentina. *Palaeogeography, Palaeoclimatology, Palaeoecology*, 492, 104–125. <https://doi.org/10.1016/j.palaeo.2017.12.017>
- Ramos, V. A., Cegarra, M., & Cristallini, E. (1996). Cenozoic tectonics of the High Andes of west-central Argentina (30–36°S latitude). *Tectonophysics*, 259(1–3), 185–200. [https://doi.org/10.1016/0040-1951\(95\)00064-X](https://doi.org/10.1016/0040-1951(95)00064-X)
- Ramos, V. A., Cristallini, E. O., & Pérez, D. J. (2002). The Pampean flat-slab of the Central Andes. *Journal of South American Earth Sciences*, 15(1), 59–78. [https://doi.org/10.1016/S0895-9811\(02\)00006-8](https://doi.org/10.1016/S0895-9811(02)00006-8)
- Reiners, P. W., & Brandon, M. T. (2006). Using thermochronology to understand orogenic erosion. *Annual Review of Earth and Planetary Sciences*, 34(1), 419–466. <https://doi.org/10.1146/annurev.earth.34.031405.125202>
- Reiners, P. W., Spell, T. L., Nicolescu, S., & Zanetti, K. A. (2004). Zircon (U-Th)/He thermochronometry: He diffusion and comparisons with <sup>40</sup>Ar/<sup>39</sup>Ar dating. *Geochimica et Cosmochimica Acta*, 68(8), 1857–1887. <https://doi.org/10.1016/j.gca.2003.10.021>
- Riesner, M., Simoes, M., Carrizo, D., & Lacassin, R. (2019). Early exhumation of the Frontal Cordillera (southern central Andes) and implications for Andean mountain-building at ~33.5°S. *Scientific Reports*, 9(1), 7972. <https://doi.org/10.1038/s41598-019-44320-1>
- Ronemus, C. B., Howlett, C. J., DeCelles, P. G., Carrapa, B., & George, S. W. M. (2024). The manantiales basin, southern central Andes (~32°S), Preserves a record of late Eocene–Miocene episodic growth of an east-vergent orogenic wedge. *Tectonics*, 43(3), e2023TC008100. <https://doi.org/10.1029/2023TC008100>
- Schmitz, M. D., & Bowring, S. A. (2001). U-Pb zircon and titanite systematics of the Fish Canyon Tuff: An assessment of high-precision U-Pb geochronology and its application to young volcanic rocks. *Geochimica et Cosmochimica Acta*, 65(15), 2571–2587. [https://doi.org/10.1016/S0016-7037\(01\)00616-0](https://doi.org/10.1016/S0016-7037(01)00616-0)
- Stalder, N. F., Herman, F., Fellin, M. G., Coutand, I., Aguilar, G., Reiners, P. W., & Fox, M. (2020). The relationships between tectonics, climate and exhumation in the Central Andes (18–36°S): Evidence from low-temperature thermochronology. *Earth-Science Reviews*, 210, 103276. <https://doi.org/10.1016/j.earscirev.2020.103276>
- Stevens Goddard, A. L., Larrovere, M. A., Carrapa, B., Aciar, R. H., & Alvarado, P. (2018). Reconstructing the thermal and exhumation history of the Sierras Pampeanas through low-temperature thermochronology: A case study from the Sierra de Velasco. *GSA Bulletin*, 130(11–12), 1842–1858. <https://doi.org/10.1130/B31935.1>
- Suriano, J., Lossada, A. C., Mahoney, J. B., Tedesco, A. M., Limarino, C. O., Giambiagi, L. B., et al. (2023). The southern extension of the Eocene Andean orogeny: New sedimentary record of the foreland basin in the southern Central Andes at 32° S. *Basin Research*, 35(6), 2381–2400. <https://doi.org/10.1111/bre.12803>
- Suriano, J., Mardonez, D., Mahoney, J. B., Mescua, J. F., Giambiagi, L. B., Kimbrough, D., & Lossada, A. (2017). Uplift sequence of the Andes at 30°S: Insights from sedimentology and U/Pb dating of synorogenic deposits. *Journal of South American Earth Sciences*, 75, 11–34. <https://doi.org/10.1016/j.jsames.2017.01.004>

- Tassara, A., & Echaurren, A. (2012). Anatomy of the Andean subduction zone: Three-dimensional density model upgraded and compared against global-scale models: Anatomy of the Andean subduction zone. *Geophysical Journal International*, 189(1), 161–168. <https://doi.org/10.1111/j.1365-246X.2012.05397.x>
- Tedesco, A. M., Escosteguy, L. D., Wilson, C. G. J., Cardó, R., Giambiagi, L. B., Yamin, M. G., et al. (2024). *Hoja Geológica 3169-III/3172-IV, Barreal, provincia de San Juan. Escala 1:250.000* (p. 195). Instituto de Geología y Recursos Minerales, Servicio Geológico Minero Argentino, Boletín N° 453.
- Val, P., Venerdini, A. L., Ouimet, W., Alvarado, P., & Hoke, G. D. (2018). Tectonic control of erosion in the southern Central Andes. *Earth and Planetary Science Letters*, 482, 160–170. <https://doi.org/10.1016/j.epsl.2017.11.004>
- Yonkee, W. A. (1992). Basement-cover relations, Sevier orogenic belt, northern Utah. *Geological Society of America Bulletin*, 104(3), 280–302. [https://doi.org/10.1130/0016-7606\(1992\)104<0280:BCRSOB>2.3.CO;2](https://doi.org/10.1130/0016-7606(1992)104<0280:BCRSOB>2.3.CO;2)